catalysts

MDPI

Review

Recent Advances on Small Band Gap Semiconductor Materials ($\leq$2.1 eV) for Solar Water Splitting

Hefeng Zhang, Jiaqi Liu, Ting Xu, Wenqian Ji and Xu Zong *

Marine Engineering College, Dalian Maritime University, Linghai Road 1, Dalian 116026, China
* Correspondence: xuzong@dlmu.edu.cn

Abstract: The conversion of solar energy into renewable H_2 fuel via photoelectrochemical and photocatalytic water splitting approaches has attracted considerable attention due to its potential to solve significant energy and environmental issues. To achieve reasonable energy conversion efficiency of 10%, which is amenable to the economic feasibility of this technology, semiconductor materials, which are the main carrier for solar H_2 production, must fulfill several important criteria. One of the most important criteria is the band gap of the semiconductor material, which should be low enough to allow the efficient absorption of incident light. This is because the band gap of semiconductor material fundamentally determines the upper limit of the theoretical energy conversion efficiency of the solar conversion system. In this work, recent advances in utilizing semiconductor material with a band gap smaller than 2.1 eV instead of the simply-defined visible-light-responsive semiconductor materials toward solar H_2 production from water splitting was reviewed.

Keywords: solar energy; semiconductor; band gap; hydrogen; water splitting

check for updates

Citation: Zhang, H.; Liu, J.; Xu, T.; Ji, W.; Zong, X. Recent Advances on Small Band Gap Semiconductor Materials (≤2.1 eV) for Solar Water Splitting. *Catalysts* **2023**, *13*, 728. https://doi.org/10.3390/catal13040728

Academic Editors: Sekar Karthikeyan and Boopathy Ramasamy

Received: 18 March 2023
Revised: 6 April 2023
Accepted: 7 April 2023
Published: 12 April 2023

1. Introduction

1.1. Solar Hydrogen Production from Water Splitting with Semiconductor Materials

The increasing concern over the depletion of traditional fossil fuels and the serious environmental problems has triggered interest in the utilization of solar energy. The main features afforded by solar energy are its abundance and cleanness. It is estimated that the magnitude of the available solar energy striking the earth's surface in 1 h (4.3×10^{20} J) is even higher than that consumed on the planet in 1 year (4.1×10^{20} J) [1]. Therefore, harvesting energy in a sustainable, environment-benign, and cost-effective manner from sunlight offers an ideal approach toward fulfilling the human need for renewable energy [2,3]. However, the large disparity between the practical utilization of solar energy and its huge theoretical capacity creates a compelling need to develop credible ways to convert solar energy.

Up to now, several strategies have been proposed and developed for the conversion of solar energy into different energy forms, such as thermal energy, chemical fuels, and electricity. Among all the strategies under investigation, solar water splitting to produce hydrogen fuel on semiconductor materials has been an important research topic in the past decades [4]. Water splitting to produce H_2 and O_2 is an uphill reaction and involves a large positive Gibbs free energy change (ΔG^0) of 237 kJ/mol [5]. Therefore, it defines the unfavorable nature of the reaction under standard conditions. However, water splitting can be realized by the well-known Honda–Fujishima effect [6], which involves illuminating an n-type TiO_2 photoanode coupled with a Pt cathode at an applied bias much lower than the voltage needed for the electrolysis of water. This finding, reported in 1972, has inspired the subsequent intense research on the conversion of solar energy to H_2 fuel via water splitting.

Two approaches, photocatalytic water splitting on semiconductor photocatalyst powder and photoelectrochemical (PEC) water splitting on semiconductor film electrodes, are typically used to produce H_2, both of which can be regarded as artificial photosynthesis [7]. Figure 1 shows the general steps required for achieving water splitting via photocatalytic reactions on photocatalyst powder suspended in an aqueous solution. In the first step, when the semiconductor powder harvests incident photons with enough energy, the electrons in the valence band are excited to the conduction band, while the holes stay in the valence band of the photocatalyst. The energy difference between the valence band and the conduction band is defined as the band gap (E_g), and the energy of the incident photon must surpass the band gap of the semiconductors to allow for light absorption. In the second step, the photogenerated charges will move to the surface of the semiconductor photocatalysts before recombination. In the third step, the photogenerated electrons will reduce protons to generate H_2, and the holes will oxidize H_2O to generate O_2 on the different active sites of the photocatalyst. As the charges photogenerated on wide band gap semiconductors have high energy for the redox reactions, they are more likely to initiate photocatalytic reactions. The three steps described above merely represent the necessary steps involved in a complete photocatalytic water-splitting reaction. There are several underlying criteria for the material that has the potential to achieve water splitting. One of the most important criteria is the valence and conduction band positions of semiconductors relative to those of the water reduction and oxidation potentials. As shown in Figure 1, the bottom level of the conduction band must be more negative than the redox potential of H^+/H_2 (0 V vs. normal hydrogen electrode (NHE)), and the top level of the valence band must be more positive than the redox potential of O_2/H_2O (1.23 V vs. NHE). Therefore, finding a material with conduction and valence band positions that can match the redox potential of water splitting is crucial, which makes this research topic extremely challenging.

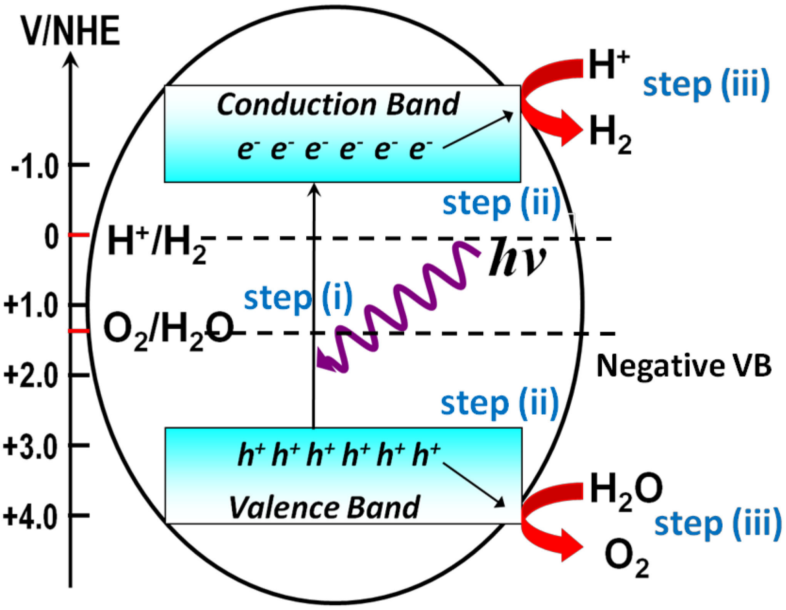

Figure 1. Schematic steps for solar H_2 production from photocatalytic water splitting.

For PEC water splitting, the general steps include creating photogenerated charges, migration of charges, and subsequent charge-induced water splitting reactions, which are quite similar to those of photocatalytic water splitting (Figure 2). However, there is one distinct difference between the two approaches. For PEC water splitting, an external potential could be applied between the working electrode made of semiconductor materials and the counter electrodes, typically made of active materials capable of catalyzing water oxidation or reduction. This applied potential will provide additional energy for the photogenerated charges and straddle the limitations that existed in photocatalytic water splitting due to the inappropriate band positions of semiconductors relative to water redox potentials. Moreover, the applied potential will provide the driving force for the directional migration of photogenerated charges, consequently decreasing their recombination and enhancing the overall efficiency of the PEC system. For example, several visible-light-responsive oxide photocatalysts, such as n-type Fe_2O_3 or WO_3 semiconductors, cannot reduce protons to produce H_2 due to their highly positive conduction band edge positions relative to the water reduction potential. However, under applied potential, photoelectrodes made of these materials can efficiently split water under visible light. Therefore, materials that are inappropriate for photocatalytic water splitting may still be qualified for PEC water splitting with the aid of applied bias. For n-type semiconductor materials, water is oxidized on the semiconductor surface and reduced on the counter electrode. Contrary to n-type semiconductor materials, water is reduced on the surface of p-type semiconductor materials and oxidized on the counter electrode.

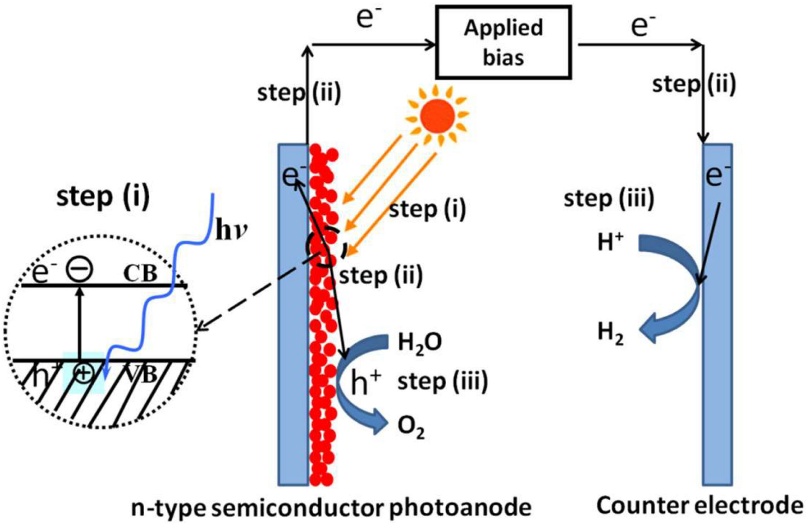

Figure 2. Schematic steps for solar H_2 production from photoelectrochemical water splitting using n-type semiconductor photoanode.

1.2. Band-Gap: The Fundamental Factor Determining the Theoretical Solar-to-H_2 (STH) Efficiency

Semiconductor materials are the main carriers for the PEC and photocatalytic reactions. Considering the general steps involved in the PEC and photocatalytic water splitting, it is evident that the semiconductors must first absorb incident photons to initiate the subsequent reactions as described by the first law of photochemistry (the Grotthuss–Draper law). The more photons semiconductors could capture, the higher efficiency the semiconductor-based reaction system could obtain. Therefore, for any semiconductor material to be potentially feasible for solar H_2 generation, it must be an excellent light harvester.

The magnitude of the band gap of a semiconductor determines the photons that could be utilized. Small band gap semiconductors harvest more photons, while wide band gap semiconductors harvest less. If we presume that all the photons with energy larger than the semiconductor band gap can be absorbed by the semiconductor and transformed to the H_2, the maximal theoretical STH efficiency of a material can be estimated from its band gap [8]. The theoretical maximal photocurrent (J_{max}) and STH efficiency of a semiconductor were fundamentally determined by its band gap. It was found that the theoretical STH obtained on anatase TiO_2 (3.2 eV), monoclinic WO_3 (2.6 eV), and α-Fe_2O_3 (2.1 eV) were 1%, 6%, and 15%, respectively [8]. If a semiconductor can absorb light of up to 800 nm (corresponds to 1.55 eV), it could achieve a theoretical STH efficiency of 32% [8]. Therefore, semiconductors with smaller band gaps will be favorable in the actual PEC water splitting, considering its possibly higher conversion efficiency of solar energy.

Service demonstrated that the energy conversion efficiency must be $\geq$10% if the economic viability of the PEC hydrogen production can be met (the energy conversion efficiency is defined as the ratio of the amount of the energy output to the energy input) [9]. This corresponds to a band gap of ca. 2.4 eV and a threshold wavelength of ca. 520 nm [8]. Therefore, even wide-band semiconductor materials are more likely to convert absorbed photons into H_2 fuel due to the high kinetic energy of the photogenerated charges. Their application as photoanode materials is impractical due to the limited theoretical energy conversion efficiency that is incompatible with what is demanded by the practical applications. It is worth noting that the band gap of semiconductor materials should also satisfy the thermodynamic energy requirement for water splitting [10]. From the standard Gibbs free energy change of 237 kJ/mol for water splitting, the theoretical band gap of the semiconductor must be at least 1.23 eV for unassisted photocatalytic water splitting [11,12]. Moreover, considering the kinetic overpotentials for the oxygen and hydrogen evolution reactions on the semiconductor surface, the actual band gap required should be more than 1.5 eV for unassisted photocatalytic water splitting [13]. Therefore, materials with a band gap in the range of 1.5 to 2.4 eV will be potentially viable candidates for photocatalytic water splitting [14]. However, in PEC water splitting, due to the assistance of applied potential, semiconductor materials with a band gap of less than 1.23 eV are still applicable [15,16].

In terms of photocatalytic water splitting efficiency, Domen et al. suggested a tentative goal as a starting point for the research on hydrogen production using a particulate photocatalyst [17]. According to their estimations, material that can split pure water with a quantum efficiency of 30% at 600 nm is required, corresponding to a theoretical STH conversion efficiency of ca. 5% as shown in Figure 3. Even though this proposed energy conversion efficiency in photocatalytic water splitting is only half of that proposed for PEC water splitting, it is evident that the development of semiconductors with a band gap as small as 2 eV (corresponding to 600 nm) is also indispensable. Therefore, compared with PEC water splitting, the photocatalytic water splitting is a more challenging topic in terms of the energy conversion efficiency.

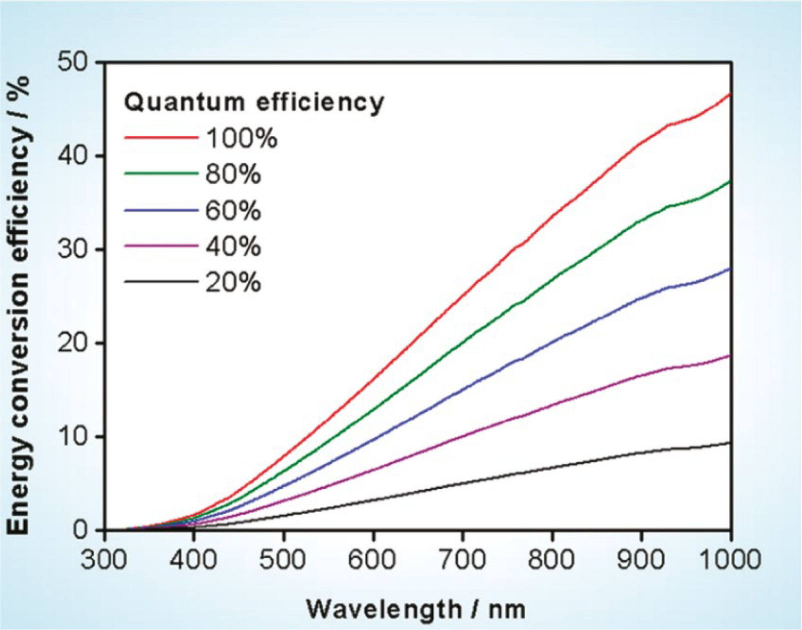

Figure 3. Calculated solar energy conversion efficiency as a function of wavelength for overall water splitting using photocatalysts with various quantum efficiencies. Solar irradiance used for the calculation was taken from AM 1.5G data. Reproduced with permission from [17]. Copyright American Chemical Society, 2010.

The aim of PEC and photocatalytic materials development is to identify a semiconductor system that has the ability to meet most, if not all, of the requirements for cost-effective solar hydrogen generation [8]. Various semiconductor nanomaterials such as oxide, sulfide and oxysulfide, nitride and oxynitride, phosphide, selenide, silicon, and silicide have been developed for solar water splitting applications. Special attention has been paid to the development of visible-light-responsive semiconductor materials (λ > 420 nm) due to their capability to utilize the larger fraction of solar electromagnetic irradiation. However, strictly speaking, from the above analysis of the maximum theoretical STH efficiency as a function of the band gap and the efficiency required in terms of economic feasibility, the development of semiconductor materials with a band gap of lower than 2.4 eV instead of simply defined visible-light-responsive materials will be highly desirable. Moreover, we should also keep in mind that when we calculate the energy conversion efficiency as a function of the band gap, we ideally assume that all the photons with energy larger than the band gap of materials can be harvested by the semiconductors to produce photogenerated charges and the photogenerated charges can be collected and converted to the H_2 fuel. Due to the unavoidable recombination of photogenerated charges and the energy loss during the conversion processes, this estimation is only ideal. If we tentatively assume 1/3 of the input energy is lost in this whole process, a theoretical energy conversion efficiency of 15% is therefore needed to achieve an actual energy conversion efficiency of 10%, which is amenable to the economic feasibility of this process. In this case, semiconductor materials with a band gap of less than 2.1 eV will be more viable candidates.

1.3. Scope of this Review Article

In recent years, owing to the rising interest in solar H_2 production from PEC and photocatalytic water splitting, significant progress has been made in this field, and several excellent reviews have been published [7,10,18–36]. However, there are still no reviews focusing on semiconductor materials with band gaps smaller than 2.1 eV. Considering the high theoretical energy conversion efficiency and correspondingly higher economic feasibility that could be obtained on small band gap semiconductor materials, it is highly desirable to give a summary of these materials. In this review article, we will provide an overview of the recent advances in the development of emerging small band gap ($E_g \leq 2.1$ eV) semiconductor materials or the modification of existing ones for solar H_2 production. Only the representative results will be discussed, and therefore, this review is not meant to be wholly thorough. Readers interested in the profile of photocatalytic and PEC water splitting could refer to other review articles and the references herein [10–16].

2. Small Band Gap ($E_g \leq 2.1$ eV) Semiconductor Materials for Solar H_2 Production

Generally speaking, the conduction band of a semiconductor material is composed of the metal element's orbitals, while the valence band is composed of the non-metal element's orbitals, except for a few cases that the metal element's orbitals can also form the valence bands. Therefore, the band gap of semiconductor material is fundamentally determined by the elements that constitute the materials. Kudo et al. gave an excellent summary of these elements in terms of their functionalities [37].

At present, oxide-based semiconductor materials account for the main part of the heterogeneous photocatalysts or photoelectrode materials under investigation. For oxide-based semiconductor materials composed of fixed metal cations, in most cases, the band gap of the materials will be decreased by replacing the oxygen elements with other non-metal elements such as nitrogen, sulfur, phosphorus, selenium, and iodine, among others. This is because the valence band positions of the resulting materials will be elevated relative to that of the oxides, where the valence band is usually composed of O 2p orbitals. At the same time, the conduction band position of the resulting materials composed of metal orbitals will remain relatively stable. Therefore, the valence band modification of semiconductor materials with various non-metal elements will bring a pronounced effect on the amplitude of the band gaps and will lead to the formation of semiconductor materials with much-reduced band gaps. In the following section, we will summarize small band gap semiconductor materials according to the main non-metal elements in the semiconductor materials.

2.1. Oxide-Based Semiconductor Materials

2.1.1. α-Fe_2O_3 (Hematite)

Hematite has a band gap of ca. 2.1 eV and theoretical STH efficiency of 15%. The conduction band position of hematite is lower than the water reduction potential; therefore, hematite cannot split pure water photocatalytically. However, hematite is one of the most promising semiconductor materials for PEC water splitting due to its attractive advantages, such as wide light absorption, low cost, excellent chemical durability, and environmental compatibility. Fe is among the most available elements that can be relied upon for the large-scale fabrication of devices [38]. However, hematite has some inherent disadvantages, such as a short minority carrier lifetime (ca. 10 ps), unsuitable conduction band energy level for H_2 production, poor conductivity, short hole diffusion distance (ca. 2 to 4 nm), and poor surface oxygen evolution reaction kinetics, which leads to much lower STH efficiency compared to the theoretical value [39,40]. Major efforts have been devoted to addressing these problems. Several methods, including elemental doping, nanostructuring, and loading of oxygen evolution catalysts, have been used to tune the electronic and structural characteristics of hematite film, and significant progress has been made [41–51]. As the synthesis, characterization, charge carrier dynamics, and photoelectrochemical properties of hematite were comprehensively reviewed in papers [52–58], we will only introduce some representative results for highly efficient hematite photoelectrode.

Gratzel and Sivula et al. extensively investigated the preparation of hematite photoanodes for PEC water splitting. They reported a highly efficient nanostructured Si-doped hematite electrode. The hematite film was deposited on a conductive FTO substrate by atmospheric pressure chemical vapor deposition from Fe $(CO)_5$ and tetraethoxysilane at 688 K [59,60]. The as-deposited film consisted of a perpendicularly oriented dendritic structure of 500 nm thickness with a feature size of only 10–20 nm at the surface. Under AM 1.5G illumination (100 mW cm^{-2}), the hematite film delivered a photocurrent density of 2.3 mA cm^{-2} in 1 M NaOH electrolyte, much higher than without Si doping (10 μA cm^{-2}). Moreover, the treatment of the hematite film with cobalt further increased the current density to 2.7 mA cm^{-2} due to enhanced water oxidation dynamics by the cobalt cocatalyst. The high efficiency achieved in this hematite film is supposed to be due to the beneficial advantages afforded by the dendritic nanostructure, which permits efficient light absorption while reducing the length that photogenerated holes have to diffuse to reach the hematite/electrolyte interface. In the following work, by optimizing the preparation conditions, hematite film with similar nanostructures while higher thickness was obtained [59]. IrO_2 nanoparticles were then loaded on the hematite surface by electrophoresis method. The loading of IrO_2 cocatalyst was found to lead to a dramatic shift of the onset potential from +1.0 V to 0.8 V vs. reversible hydrogen electrode (RHE). Moreover, a high photocurrent of over 3 mA cm^{-2} was achieved with this hematite electrode at 1.23 V vs. RHE under AM 1.5G 100 mW cm^{-2} simulated sunlight illuminations due to the improved nanostructure and catalytic properties of the hematite film. The important role of cocatalysts in improving the PEC performance of hematite has also been investigated by other groups from both experimental and fundamental aspects [45,61,62]. Gratzel and Sivula et al. also developed several strategies for the low-cost preparation of hematite film, the confinement of the feature size of hematite film nanoparticles, and surface modification with oxide layers to improve the onset potential for water oxidation [44,63,64].

Li et al. developed a series of low-cost and facile approaches for fabricating highly efficient hematite photoanodes such as Sn-doped, Ti-doped, and oxygen-deficient hematite [41,65,66]. Hydrothermal and subsequent high-temperature sintering in air was used to prepare Sn-doped hematite nanowires or nanocorals films on FTO substrate [41]. Photocurrents of 1.24 and 1.86 mA cm^{-2} were achieved at 1.23 V vs. RHE on the nanowire film and nanocoral films, respectively. Compared with undoped hematite nanostructures, the Sn-doped ones showed remarkable photocurrent densities due to the enhanced conductivity and surface area by Sn doping. To prepare a Ti-doped hematite photoelectrode, a facile deposition-annealing (DA) process was used, during which iron (III) chloride and titanium butoxide were used as the Fe and Ti precursors, respectively [65]. An annealing at a temperature as low as 823 K was used. Under optimized conditions, the Ti-doped hematite film achieved a photocurrent density of 2.8 mA cm^{-2} at 1.23 V vs. RHE (Figure 4). Impedance measurements exhibit that the Ti-dopant acts as an electron donor and improves the donor density by two orders of magnitude. The increased photocurrent is ascribed to the increased donor density and decreased electron-hole recombination due to the Ti doping. Moreover, Li's group prepared a highly efficient oxygen-deficient hematite photoelectrode by thermal treatment of akaganeite nanowire arrays in an oxygen-deficient environment at a quite low activation temperature of 823 K [66]. The as-prepared hematite electrode delivered a photocurrent density of 3.37 mA cm^{-2} at 1.50 V vs. RHE. The drastic enhancement of the PEC performance of the hematite film is due to the enhanced donor density originating from the formation of an oxygen vacancy (Fe^{2+}). This work showed a simple and effective method for the preparation of highly photoactive undoped hematite at a relatively low activation temperature for PEC water splitting.

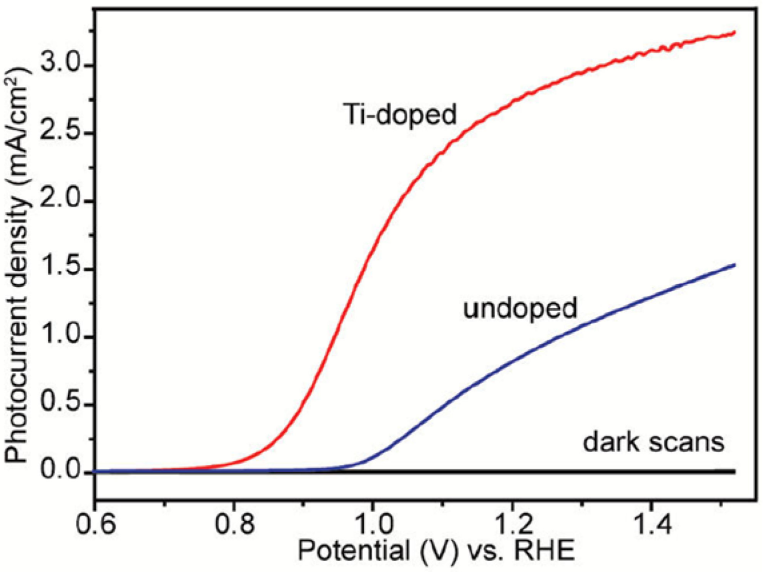

Figure 4. Comparison of photocurrent densities collected for optimized undoped and Ti-doped hematite films. Reproduced with permission from [65]. Copyright American Chemical Society, 2011.

2.1.2. Cu_2O

Cuprous oxide, Cu_2O, has a direct band gap of 2.0 eV and a corresponding theoretical STH conversion efficiency of 18% [67]. The conduction band of Cu_2O is located at 0.7 V, negative of the water reduction potential, and the valence band is just positive of the water oxidation potential [68,69]. Therefore, from the thermodynamic point, Cu_2O can achieve the hydrogen evolution half reaction while it is ineffective for the water oxidation reaction. Furthermore, considering that the redox potentials for the reduction and oxidation of Cu_2O lie within its band gap, Cu_2O is not stable when illuminating in aqueous solutions, which severely limits its application as a photocathode material for PEC water splitting. Therefore, finding a proper coating layer that can protect a Cu_2O photoelectrode against photocathodic decomposition while allowing an efficient electron tunnel is important for this material [70–74].

Paracchino et al. developed a highly efficient and relatively stable Cu_2O photocathode for PEC water splitting [75,76]. Cu_2O film was first prepared onto FTO substrates with an electrodeposition method. Ultrathin protective layers of Al-doped ZnO and TiO_2 were then deposited onto the Cu_2O photocathode layer by layer with an atomic layer deposition technique. Finally, Pt nanoparticles were electrodeposited on the top layer of the photoelectrode to enhance the kinetics of the water reduction reaction. It was found that the cathodic photocurrent density observed on the bare Cu_2O electrode reached a plateau of 2.4 mA cm^{-2} and decreased dramatically with short-term irradiation due to the reductive decomposition of Cu_2O. However, the photocurrent density of Cu_2O with a protective layer reached 7.8 mA cm^{-2} at 0 V vs. NHE. Moreover, the stability of the Cu_2O electrode was greatly improved. The authors pointed out that the protective layer must meet several criteria. First, the protective layer must have a staggered type-II offset to allow the flow of photogenerated charges to the desirable direction. Second, the conduction band of the protective layer should be higher than the water reduction potential, and the protective layer should be stable. Third, the surface of the protective layer in contact with the electrolyte should be favorable for the water reduction reactions. By tuning the deposition conditions of the protective layer, a highly efficient Cu_2O photocathode was obtained in this study. Even the Cu_2O photocathode degraded with prolonged irradiation; the authors expected that its stability could be further improved by optimizing the building block material for the protective layer.

To address the photocorrosion problem on the Cu_2O photocathode, Zhang and Dua et al. developed a facile strategy [77]. In their approach, a glucose solution was first coated onto the Cu_2O nanowire array electrode. A subsequent carbonization treatment will decompose glucose to form a protective carbon coating onto the Cu_2O electrode. The thickness of the carbon layer was tuned by changing the concentration of the glucose solution. After depositing the carbon layer on the Cu_2O, the as-obtained electrode exhibited remarkably improved photostability as well as considerably enhanced photocurrent density. Under optimum conditions, carbon-layer protected Cu_2O nanowire arrays delivered a photocurrent density of 3.95 mA cm^{-2} and an energy conversion efficiency of 0.56% under AM 1.5 G illumination (100 mW cm^{-2}). Compared with the atomic layer deposition strategy mentioned above, this strategy is much more facile and inexpensive and will provide a general approach that can mitigate the stability problem of many nonstable photoelectrodes.

To improve the stability of the Cu_2O electrode, Lin deposited NiO_x cocatalyst film onto the Cu_2O nanowire electrode [78]. In this work, a NiO_x precursor solution was first spin-coated onto a Cu_2O electrode. Subsequent annealing of the Cu_2O electrode in air will decompose the NiO_x precursor to NiO_x cocatalyst. After loading the NiO_x cocatalyst, a photocurrent density of −0.56 mA cm^{-2} at 0.1 V vs. NHE was obtained under light irradiation (26 mW cm^{-2}). Moreover, the NiO_x-modified Cu_2O electrode showed greatly improved stability compared with the bare ones. The authors suppose the photogenerated electrons will transfer from the Cu_2O to NiO_x cocatalyst and reduce NiO_x to metallic Ni. Metallic Ni will act as the H_2 evolution cocatalyst and is re-oxidized to Ni^{2+}. Therefore, the deposition of NiO_x on Cu_2O can significantly improve the water reduction reaction dynamics and simultaneously improve the stability of Cu_2O.

2.1.3. $CuNbO_3$ and $CuNb_3O_8$

Maggard's group developed a series of novel Cu^+-based semiconductor materials such as $CuNbO_3$, $CuNb_3O_8$, $CuNb_{13}O_{33}$, $Cu_5Ta_{11}O_{30}$, and $Cu_3Ta_7O_{19}$ and systematically investigated their PEC performance for water-splitting [79–82]. All these materials are visible light responsive. However, only $CuNbO_3$ and $CuNb_3O_8$ have band gaps of less than 2.1 eV. $CuNbO_3$ and $CuNb_3O_8$ powder were synthesized by heating a stoichiometric mixture of Cu_2O and Nb_2O_5 in an evacuated fused silica tube at the proper temperature and duration. The photocathodes were then prepared by spreading the as-synthesized powder onto FTO conductive substrate with post-heat treatment under a vacuum. $CuNbO_3$ is a red color p-type semiconductor with a band gap of ca. 2.0 eV [79]. Density functional theory calculations show the visible light absorption results from a nearly direct band gap transition owing mainly to copper-to-niobium excitations. Figure 5 shows the current-potential curve of the $CuNbO_3$ photocathode under chopped visible light illumination ($\lambda > 420$ nm). It was found that the $CuNbO_3$ photocathode exhibited an onset potential of +0.10 V vs. saturated calomel electrode (SCE) and achieved a cathodic photocurrent of −0.10 mA cm^{-2} at −0.6 V vs. SCE. The incident photon-to-current conversion efficiency (IPCE) of ca. 1–2% is attained at the lowest visible-light energies and rises sharply to >5%

at higher incident photon energies. Moreover, the p-type $CuNbO_3$ film exhibited a stable photocurrent and notable resistance to photocorrosion.

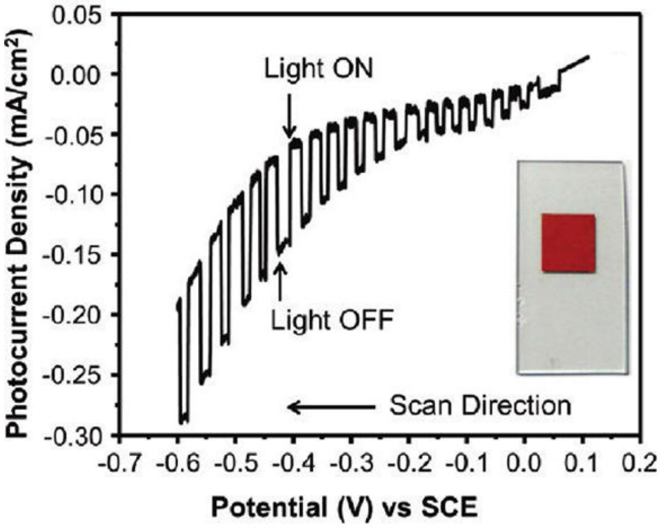

Figure 5. The current-potential curve in an aqueous 0.5 M Na_2SO_4 solution (pH 6.3) under chopped visible-light irradiation (λ > 420 nm) for a $CuNbO_3$ electrode. Insert shows a photograph of the $CuNbO_3$ film on FTO glass. Reproduced with permission from [79]. Copyright 2011, American Chemical Society.

Similar to $CuNbO_3$, $CuNb_3O_8$ has a p-type property [80]. However, because of the different crystal structures, $CuNb_3O_8$ was found to have indirect and direct band gap values of 1.26 and 1.47 eV and consequently can utilize a larger fraction of the solar irradiation. Furthermore, the conduction and valence bands of $CuNb_3O_8$ are higher than the water reduction and oxidation potentials, respectively. As a result, $CuNb_3O_8$ can thermodynamically reduce water to H_2 but not oxidize it to O_2. Under visible light irradiation (λ > 420 nm), the $CuNb_3O_8$ photocathode showed an onset potential of +0.30 V vs. RHE and a cathodic photocurrent of -0.40 mA cm^{-2} at -0.35 V vs. SCE. Moreover, this p-type $CuNb_3O_8$ film also exhibited a stable photocurrent. The above studies indicated that $CuNbO_3$ and $CuNb_3O_8$ are potentially good candidates for fabricating photocathodes for PEC water splitting due to their excellent light absorption properties, suitable conduction band edge position, and relatively high stability against photocorrosion.

2.1.4. $CaFe_2O_4$

$CaFe_2O_4$, a p-type semiconductor material, has a band gap of 1.9 eV. The conduction and valence band edges of $CaFe_2O_4$ are located at -0.6 and +1.3 V vs. NHE, respectively, fulfilling the thermodynamic requirement for the hydrogen and oxygen evolution reactions [83–85]. Ida et al. reported the fabrication of a p-type $CaFe_2O_4$ photocathode for water splitting [86]. The $CaFe_2O_4$ photocathode was prepared by spreading $CaFe_2O_4$ powder onto a Pt plate followed by annealing at 1373–1473 K for 2 h. The $CaFe_2O_4$ photocathode prepared at 1373 K consisted of powder with particle sizes of 2–4 μm, while annealing at 1473 K will melt the powder to form a (hk0)-oriented $CaFe_2O_4$ planar film. The electrode prepared at 1473 K presented a photocurrent that was ca. 10–50 times higher than the electrode prepared at 1373 K due to the improvements in film quality and the better contact between the $CaFe_2O_4$ film and Pt substrate (Figure 6). IPCE of 5–15% and less than 5% was obtained in the UV and visible regions, respectively. A small photocurrent was also observed up to 650 nm, corresponding to the band edge of $CaFe_2O_4$. However, the photocurrent was quite low in the visible region, possibly due to the faster recombination of the as-generated electron-hole pairs. When a bias of 1 V was applied between the $CaFe_2O_4$ cathode and Pt anode in a two-electrode system under irradiation, H_2 and O_2 can be produced with a nearly stoichiometric ratio. Moreover, a photocell short-circuited by connecting the p-type $CaFe_2O_4$ and n-type TiO_2 can also split water with no applied bias under illumination. However, the ratio of H_2 to O_2 is not stoichiometric, probably attributed to the oxidation or oxygen adsorption on the TiO_2/Ti electrode. Moreover, the photocurrent of this photocell gradually decreased, possibly due to the decomposition of $CaFe_2O_4$ upon long-time illumination. This instability problem is anticipated to be solved by loading the proper cocatalyst. Following this work, Cao et al. prepared p-type $CaFe_2O_4$ nanofilms on an FTO glass substrate using a pulsed laser deposition (PLD) method. The as-prepared film showed high PEC performance for the H_2 production even without applied bias [87].

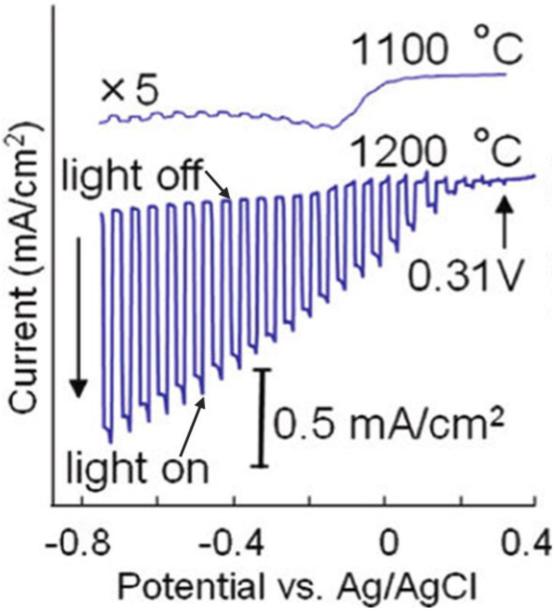

Figure 6. Current-potential curves in 0.1 M NaOH solution under chopped light illumination (500 W Xe lamp) for $CaFe_2O_4$ electrodes treated at 1473 and 1373 K. Reproduced with permission from [86]. Copyright American Chemical Society, 2010.

2.1.5. $Sr_{1-x}NbO_3$ ($0.1 \leq x \leq 0.2$)

Xu et al. reported the synthesis of a series of red oxide semiconductors with a chemical formula of $Sr_{1-x}NbO_3$ ($0.1 \leq x \leq 0.2$) and their properties for the photocatalytic water splitting reaction under visible irradiation [88]. The absorption edges of the $Sr_{1-x}NbO_3$ ($0.1 \leq x \leq 0.2$) catalysts are located at ca. 700 nm, corresponding to a band gap of 1.9 eV. Furthermore, the band gaps of $Sr_{1-x}NbO_3$ ($0.1 \leq x \leq 0.2$) catalysts reduce gradually with reducing Sr content. Under visible light illumination, the $Sr_{1-x}NbO_3$ catalysts displayed activity for the oxidation and reduction of water in the presence of suitable sacrificial reagents, indicating the proper band edge positions of $Sr_{1-x}NbO_3$ relative to both the hydrogen and oxygen evolution potentials. Furthermore, the photocatalytic activity of $Sr_{1-x}NbO_3$ can be further enhanced by ball milling treatment due to the resulting increased surface area. One interesting property of the $Sr_{1-x}NbO_3$ materials is their high electronic conductivity of ca. 3×10^3 S cm^{-1} ($x = 0.2$), which indicates their metallic nature instead of that observed in traditional semiconductor photocatalysts. The authors suggested that the absorption of the photons was due to the excitation from the partially filled conduction band to a higher-level unoccupied band. Although the exact origin of the light absorption needs to be further investigated, the wide absorption up to 700 nm, the appropriate energy level, and the high conductivity may entail $Sr_{1-x}NbO_3$ a promising candidate for PEC water splitting.

2.2. Nitride and Oxynitride-Based Semiconductor Materials

Domen's group developed a series of Ta, Nb, Ti, Ga, and Ge-based nitride and oxynitride semiconductor materials for photocatalytic and PEC water splitting. The tops of the valence bands of these materials consist primarily of N 2p orbitals or O 2p hybridized N 2p orbitals, and the bottoms of the conduction band consist of metal orbitals. Compared with oxide materials, the corresponding nitride or oxynitride materials will have much-reduced band gaps due to the contribution of N 2p orbitals to the valence band. Moreover, compared with sulfide materials, nitride or oxynitride materials exhibited relatively high stability against photo corrosion, forming a unique type of visible-light-responsive semiconductor material.

2.2.1. Ta_3N_5

Ta_3N_5 is one of the most investigated nitride semiconductor materials for photocatalytic and PEC water-splitting applications [89–92]. Ta_3N_5 has several important features that are compatible with solar water-splitting reactions. For example, Ta_3N_5 has a small band gap of around 2.1 eV and can achieve a maximum theoretical energy conversion efficiency of 15.9%. This property is comparable with that of Fe_2O_3. Moreover, the conduction and valence band levels of Ta_3N_5 are located at ca. +1.6 V and −0.4 V vs. NHE at pH = 0, respectively, and therefore can fulfill the thermodynamic requirement for both water reduction and oxidation reactions.

Ta_3N_5 was initially investigated as a photocatalyst for photocatalytic water-splitting reactions [89,90,93–100]. It was prepared by heating Ta_2O_5 powder in an NH_3 flow at 1123 K. Under visible light irradiation, Ta_3N_5 can reduce water to produce H_2 in an aqueous methanol solution. Moreover, Ta_3N_5 can produce O_2 via water oxidation with $AgNO_3$ as a sacrificial reagent. Even though the efficiency achieved on Ta_3N_5 for photocatalytic water splitting is low in the presence of sacrificial reagents, it represents one of the quite few materials with a band gap of 2.1 eV together with the ability to split water without applied bias. The photocatalytic activity of Ta_3N_5 for water oxidation was improved by six times via modifying Ta_3N_5 with alkaline metal salts [101], indicating the potential of further improving the photocatalytic performance of Ta_3N_5 with the proper synthesis technique.

Apart from photocatalytic water splitting, Ta_3N_5 has been extensively investigated as a photoanode material for PEC water oxidation [102,103]. Abe et al. used a simple electrophoretic deposition method for the fabrication of a Ta_3N_5 photoelectrode [104]. In this approach, Ta_3N_5 powder was first prepared and then assembled on the FTO substrate with the electrophoretic deposition method. This as-deposited Ta_3N_5 photoelectrode showed negligible photocurrent. Then a post-necking treatment of the Ta_3N_5 photoelectrode in NH_3 was employed to ensure better contact between the Ta_3N_5 powder and the Ta_3N_5 powder with the FTO substrate. The as-prepared film demonstrated drastically enhanced photocurrent after this post-necking treatment. The loading of IrO_2 as a cocatalyst on Ta_3N_5 was found to further drastically enhance the photocurrent by more than three times using Na_2SO_4 as the electrolyte. However, the Ta_3N_5 photoelectrode degraded upon light irradiation due to self-photooxidation. The stability of the Ta_3N_5 photoelectrode was significantly improved by using a Co_3O_4 nanoparticle water oxidation cocatalyst and an alkaline electrolyte [105].

In order to further promote the PEC performance of Ta_3N_5, several strategies have been used to prepare the Ta_3N_5 photoanode [106–116]. Li et al. reported the preparation of vertically aligned Ta_3N_5 nanorod arrays via nitridation of Ta_2O_5 nanorod arrays prepared in situ on Ta foil using a through-mask anodization approach (Figure 7). The as-prepared Ta_3N_5 electrode exhibited a photocurrent density of 3.8 mA cm^{-2} at an applied potential of 1.23 V vs. RHE under AM 1.5G simulated sunlight at 100 mW cm^{-2} and a maximum IPCE of 41.3% at 440 nm. This current density is 3.2 times higher than that of a thin film Ta_3N_5 photoelectrode. Moreover, by coating the Co-Pi cocatalyst on Ta_3N_5 nanorod arrays, the Ta_3N_5 electrode demonstrated quite high stability during the PEC reactions [110]. Zhen et al. reported the simple template-free synthesis of a Ta_3N_5 nanorod array on Ta substrate by combining a vapor-phase hydrothermal process and subsequent nitriding. After modification with a Co $(OH)_x$ cocatalyst, the Ta_3N_5 nanorod array films exhibited a stable photocurrent density of 2.8 mA cm^{-2} at 1.23 V vs. RHE under AM 1.5G simulated sunlight. The IPCE at 480 nm is ca. 37.8% [109].

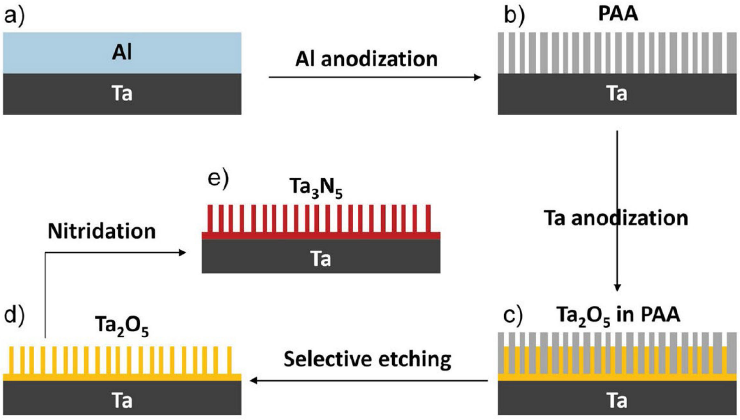

Figure 7. Schematic process for the fabrication of vertically aligned Ta_3N_5 nanorod array. (**a**) Al layer coated on a clean Ta substrate by thermal evaporation. (**b**) PAA mask formed by anodizing the Al layer in 0.3 M oxalic acid. (**c**) Ta_2O_5 nanorods embedded in the PAA mask by anodizing the Ta substrate through the PAA mask in 0.5 M boric acid. (**d**) Ta_2O_5 nanorod array obtained by selectively etching the PAA mask with 5% phosphoric acid. (**e**) Ta_3N_5 nanorod array obtained by nitridation of the Ta_2O_5 nanorod array in an NH_3 atmosphere. Reproduced with permission from [110]. Copyright WILEY-VCH Verlag GmbH & Co. KGaA, Weinheim, 2013.

2.2.2. $MTaO_2N$ (M = Sr, Ba)

A series of alkaline earth tantalum oxynitrides with a chemical formula of $MTaO_2N$ (M = Ca, Sr, Ba) have been developed for photocatalytic water-splitting reactions. Among these materials, $SrTaO_2N$ and $BaTaO_2N$ have band gaps of 2.1 and 2.0 eV, respectively [117–120]. The conduction band and valence band compositions for both materials are the same as that of Ta_3N_5, while the participation of Sr and Ba will lead to different electronic structures [121–124]. Both materials can generate H_2 from an aqueous methanol solution under visible light. Under visible light irradiation, $SrTaO_2N$ will undergo self-oxidative decomposition in the presence of I^- and unsuitable in the Z-scheme system, while $Pt/BaTaO_2N$ can split pure water when used as an H_2-evolution photocatalyst in combination with a Pt/WO_3 photocatalyst in a Z-scheme system. Moreover, Pt-$BaTaO_2N$ is also reported to be photoactive at wavelengths up to 660 nm, representing the first example of an overall water-splitting system where visible light at wavelengths longer than 600 nm is effectively absorbed for H_2 evolution [125,126].

2.2.3. $LaTiO_2N$

Ti-based oxynitride, $LaTiO_2N$, has a band gap of 2.1 eV [127,128]. The top of the valence band consists predominantly of N 2p orbitals with a small contribution from O 2p orbitals, while the bottom of the conduction band is composed of empty Ti 3d orbitals. The conduction and valence bands of $LaTiO_2N$ are suitable for water reduction and oxidation reactions, respectively. When loading Pt as a cocatalyst, $LaTiO_2N$ can produce H_2 from an aqueous methanol solution under visible light irradiation. Moreover, $LaTiO_2N$ showed activity for photocatalytic O_2 production with $AgNO_3$ as the sacrificial reagent [129–132]. $LaTiO_2N$ with both single-crystalline mesoporous and macroporous architectures was prepared and then modified with a CoO_x cocatalyst. The as-obtained $CoO_x/LaTiO_2N$ photocatalyst demonstrated drastically enhanced efficiency for photocatalytic water oxidation reactions. A quantum efficiency of 27.1 ± 2.6% at 440 nm was achieved on the optimized $CoO_x/LaTiO_2N$ photocatalyst [133].

$LaTiO_2N$ has also been investigated as a photoanode material for PEC water splitting [134,135]. Domen's group proposed a particle transfer (PT) approach for fabricating $LaTiO_2N$ photoelectrodes [136,137]. $LaTiO_2N$ powder was first coated onto a primary glass substrate. A thin contact layer and a thick contact layer were subsequently deposited onto the $LaTiO_2N$ layer with radio-frequency (RF) magnetron sputtering. The above three layers were adhered to a second glass plate by epoxy resin, then peeled off the primary glass plate. Even though this approach requires complex procedures and facilities, it will ensure good electrical contact with the semiconductor particles and facilitate the charge transfer. Under AM 1.5G irradiation, a photocurrent of ca. 3 mA cm^{-2} at 1.23 V_{RHE} and nearly 100% Faradic efficiency was obtained, much higher than that obtained with the previous method. The problem with this material is its relatively low stability during the PEC reactions, even though it was modified with IrO_2 as the oxygen evolution cocatalyst.

2.3. Sulfide and Oxysulfide-Based Semiconductor Materials

2.3.1. $CuInS_2$

Copper indium disulfide ($CuInS_2$) has a band gap of ca. 1.5 eV and a large absorption coefficient (ca. 10^5 cm^{-1}) [138]. The conduction band of $CuInS_2$ is suitable for the water reduction reaction, while the valence band is unsuitable for the water oxidation reaction [139,140]. Xie et al. investigated the photocatalytic H_2 production on $CuInS_2$ powder prepared by a facile solvothermal method. The as-obtained $CuInS_2$ powder exhibited monodisperse hierarchical microarchitectures. Under visible light irradiation, the Pt/$CuInS_2$ powder can produce H_2 at 20 µmol h^{-1} with Na_2S-Na_2SO_3 as sacrificial reagents [141]. Ikeda et al. investigated PEC water splitting on a modified $CuInS_2$ photocathode [142]. The $CuInS_2$ photocathode was synthesized from electrochemically stacked metallic Cu and In layers followed by sulfurization. A Cu/In ratio of 1.3–1.4 was used to obtain $CuInS_2$ film with high crystallinity and large grain sizes. The bare $CuInS_2$ photocathode showed negligible cathodic photocurrent under illumination. After loading the Pt cocatalyst, the $CuInS_2$ photocathode showed drastically enhanced photocurrent. The introduction of an n-type buffer layer, such as CdS and ZnS, on the $CuInS_2$ photocathode before the Pt loading will further enhance the performance of the $CuInS_2$ photoelectrode (Figure 8). IPCE as high as 20% at wavelengths ranging from 500 to 750 nm was obtained.

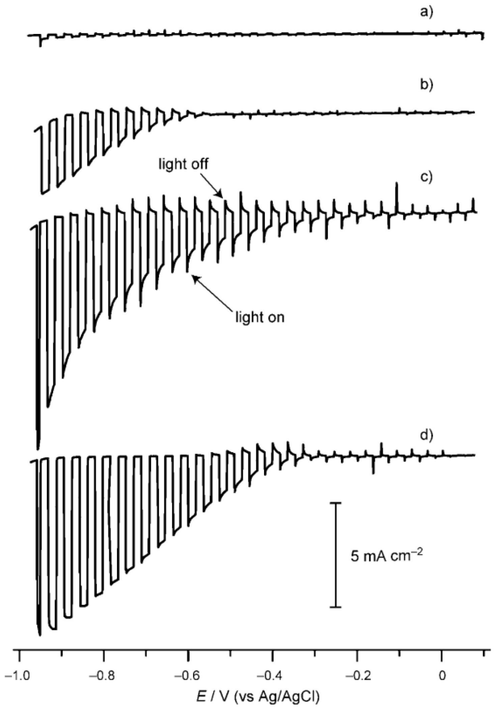

Figure 8. Current density vs. potential scans of (**a**) $CuInS_2$, (**b**) Pt-$CuInS_2$, (**c**) Pt-CdS/$CuInS_2$, and (**d**) Pt-ZnS/$CuInS_2$ in a Na_2SO_4 solution with pH adjusted to 4 under chopped illumination from a Xe lamp. Reproduced with permission from [142]. Copyright WILEY-VCH Verlag GmbH & Co. KGaA, Weinheim, 2011.

2.3.2. $Ln_2Ti_2S_2O_5$ (Ln = Pr, Nd, Sm, Gd, Tb, Dy, Ho, and Er)

Domen et al. systematically investigated a series of Ti, Ga, and In-based oxysulfide materials for photocatalytic water splitting due to their strong absorption in the visible region [143–148]. $Sm_2Ti_2S_2O_5$ is the first reported oxysulfide material capable of splitting water photocatalytically in the presence of sacrificial reagents [143]. It was prepared by heating a stoichiometric mixture of Sm_2S_3, Sm_2O_3, and TiO_2 in a sealed vacuum quartz tube at 1273 K [143]. The band gap of the resulting $Sm_2Ti_2S_2O_5$ was determined to be ca. 2.0 eV from the UV-Vis spectra, which is much smaller than that of $Sm_2Ti_2O_7$ (Figure 9). DFT calculations indicated that the contribution of the S 3p orbitals to the top part of the valence band of $Sm_2Ti_2S_2O_5$ led to a smaller band gap. Under visible light irradiation ($\lambda > 420$ nm), $Sm_2Ti_2S_2O_5$ can reduce water to produce H_2 from aqueous solutions containing sacrificial electron donors (Na_2S-Na_2SO_3 or methanol). More interestingly, when loaded with IrO_2 cocatalyst, $Sm_2Ti_2S_2O_5$ can also oxidize water to produce O_2 in the presence of a $AgNO_3$ sacrificial reagent. This property of oxysulfide is unique when compared with sulfide materials that are incapable of oxidizing water due to the instability problem. PEC measurement indicated that $Sm_2Ti_2S_2O_5$ was an n-type material and showed a quite small photocurrent for PEC water splitting. From these results, the conduction and valence band edge levels of $Sm_2Ti_2S_2O_5$ are determined to be suitable for water reduction and oxidation reactions. Moreover, the flat band potential of $Sm_2Ti_2S_2O_5$ was found to be almost independent of pH, which is similar to that of sulfide material but totally different from that of oxide material. The problem with the $Sm_2Ti_2S_2O_5$ material is its low efficiency for photocatalytic water splitting. In the subsequent work, the modification of $Sm_2Ti_2S_2O_5$ with metal ions such as Ag^+ and Mg^{2+} was found to increase the photocatalytic activity of $Sm_2Ti_2S_2O_5$ by seven times [148,149]. Similar to $Sm_2Ti_2S_2O_5$, a series of Ti-based oxysulfide materials with a chemical formula of $Ln_2Ti_2S_2O_5$ (Ln = Pr, Nd, Sm, Gd, Tb, Dy, Ho, and Er) with band gaps of 1.9–2.1 eV were synthesized and demonstrated photocatalytic activity for the water reduction and oxidation reactions in the presence of sacrificial reagents, respectively [145].

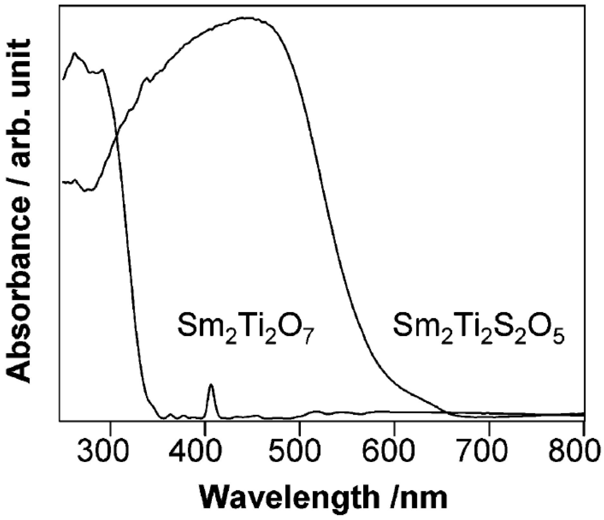

Figure 9. UV-Vis diffuse reflectance spectra for $Sm_2Ti_2O_7$ and $Sm_2Ti_2S_2O_5$. Reproduced with permission from [143]. Copyright American Chemical Society, 2002.

2.4. Selenide-Based Semiconductor Materials

2.4.1. $CuIn_{1\text{-}x}Ga_xSe_2$ (CIGS)

CIGS are a series of small band gap semiconductor materials. By tuning the ratios of In and Ga, the resulting materials will have band gaps ranging from 1.0 to 1.7 eV. These materials have several attractive properties for solar energy conversion applications, including good carrier transport properties and a direct band gap [29,150]. The conduction band edge level of $CuIn_{1\text{-}x}Ga_xSe_2$ is high enough for the hydrogen evolution reaction, while the valence band edge level is too shallow for oxide water. Marsen et al. reported the preparation of semitransparent $CuGaSe_2$ film [151]. The 0.9 μm thick films were grown on an FTO substrate by vacuum coevaporation of elemental Cu, Ga, and Se and showed polycrystalline structures with grain sizes of tens of nanometers. Under outdoor one sun irradiation, the as-prepared $CuGaSe_2$ photocathode showed a photocurrent density of up to 13 mA cm^{-2}. Significant IPCE throughout the visible spectrum, peaking at 63% at 640 mm, was obtained. Moreover, under AM 1.5G light irradiation, the $CuGaSe_2$ photocathode showed a notably stable photocurrent, indicating the high stability nature of the film at cathodic potentials (Figure 10). Similar results were obtained in other studies [152]. Yokoyama et al. reported the preparation of CIGS films onto Mo-coated soda-lime glass using a molecular beam epitaxy apparatus [153]. They observed a similar phenomenon in the $CuGaSe_2$ film mentioned above. Under irradiation by monochromatic light (λ = 600 nm), the IPCE of CIGS, Pt/CIGS, and Pt/CdS/CIGS were 0.03, 19, and 59%, respectively, at −0.24 V vs. RHE. Although all the above studies claim that CIGS is a good candidate for practical water splitting, the high cost of In and Ga will be a big barrier toward this goal.

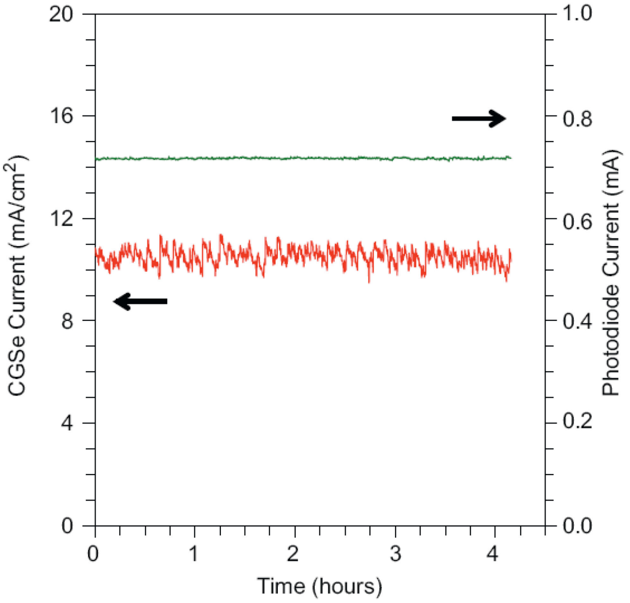

Figure 10. Four-hour test under simulated AM 1.5G light at −0.9 V vs. SCE for $CuGaSe_2$ photocathode. Photodiode current shows constant light intensity. Reproduced with permission from [151]. Copyright Elsevier B.V., 2008.

2.4.2. WSe_2

Tungsten diselenide (WSe_2) is a layered semiconductor material with a direct band gap of 1.4 eV and an indirect band gap of 1.2 eV. WSe_2 has been traditionally investigated as a photoanode material for PEC water splitting. It was reported that n-type WSe_2 had shown stability and attractive >17% PEC energy conversion efficiency in aqueous polyhalide-based redox systems [154]. Due to the excellent properties of WSe_2, Mckone et al. fabricated p-type WSe_2 photocathodes and investigated their performance for PEC water splitting [155]. In their work, crystalline p-type WSe_2 crystals were first grown using a chemical vapor transport method. The as-grown crystals were then cut into small pieces and used as the photocathode after proper treatment. To enhance the performance of the WSe_2, Ru and Pt cocatalysts were deposited onto WSe_2 using a photo-electrochemical method. PEC measurements showed that the bare p-type WSe_2 photocathode exhibited negligible photocurrent density, indicating the photocathodes produced negligible net conversion of light energy to H_2. However, after Ru or Pt cocatalyst loading, the p-type WSe_2 photocathode exhibited drastically enhanced photocurrent of up to 24 mA cm^{-2} at 0 V vs. RHE under AM 1.5G illumination (Figure 11). Overall thermodynamic photoelectrode solar energy-conversion efficiency of >7% was achieved using the Pt-Ru composite catalysts on the p-type WSe_2 photocathode. Moreover, the p-type WSe_2 photocathode demonstrated high stability under cathodic conditions for at least 2 h in both acidic and alkaline electrolytes. The problem for the p-type WSe_2 photocathode is the short effective minority-carrier diffusion lengths of only ca. 1 μm, which results in low quantum efficiencies at photon energies below the direct band gap. It was suggested that higher energy conversion efficiencies could be achieved with enhanced doping control and further improvements in crystal purity [156–158].

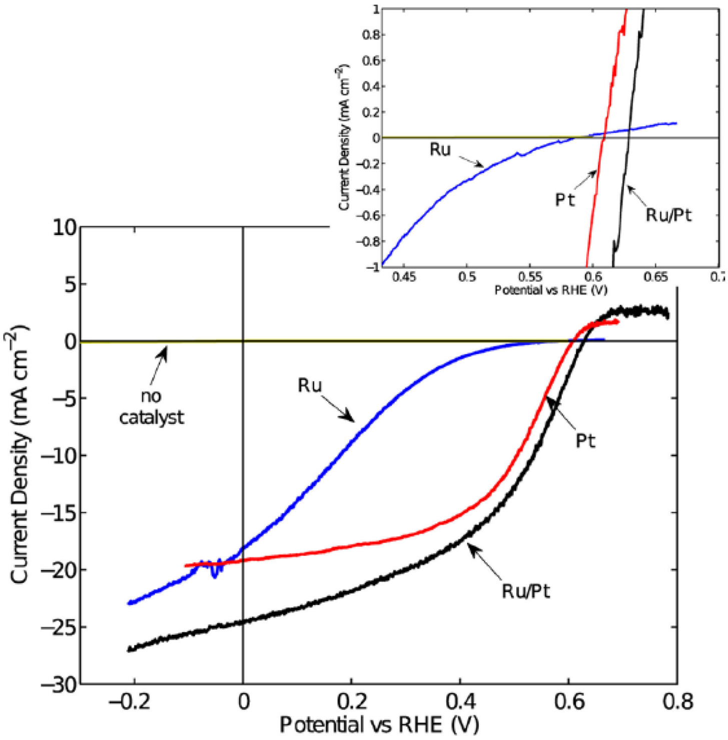

Figure 11. J–E behavior of the p-WSe_2 photoelectrodes generating H_2 from aqueous pH 4.2 electrolyte without catalyst coating and with Ru, Pt, or Ru/Pt coatings, respectively. All electrodes were illuminated using an ELH tungsten halogen lamp calibrated to an equivalent of 100 mW cm^{-2} intensity using a Si photodiode. The inset is a detail of the region around the open-circuit potential of the photoelectrodes. Reproduced with permission from [155]. Copyright American Chemical Society, 2013.

2.5. Phosphide-Based Semiconductor Materials

InP

InP is an important material with a band gap of 1.3 eV. InP's conduction band edge level is more negative than the hydrogen evolution potential, fulfilling the thermodynamic requirement for the water reduction reactions [159,160]. InP has been investigated as a photocathode semiconductor for PEC water splitting, and an energy conversion efficiency of ca. 12% has been obtained in the InP photocathode [161]. Lee et al. investigated the effect of nanostructuring on the PEC performance of InP photocathode for PEC water splitting [162]. Figure 12 shows the process flow for the fabrication of InP nanopillar arrays. InP nanopillars were first obtained by treating planar p-type InP (100) bulk wafer with a reactive ion etching and surface cleaning process. A TiO_2 passivation layer was then deposited on the InP nanopillars with atomic-layer deposition (ALD) to improve the stability of InP. Finally, a Ru film with a thickness of ca. 2 nm was sputtered on the surface to act as the H_2-evolution cocatalyst. The reflectance of InP nanopillar structures was found to be drastically reduced compared to the planar InP wafer due to the nanostructuring of the surface. Under AM 1.5G illumination, the InP photocathode with nanopillar structure shows a higher current density and more positive onset potential (ca. 37 mA cm^{-2}, 0.73 V vs. NHE) than that with the planar morphology (ca. 27 mA cm^{-2}, 0.5 V vs. NHE). This high current density achieved on the InP nanopillars approaches the theoretical limit, and high energy conversion efficiency of ca. 14% was obtained. Moreover, the stability of the nanostructured InP photocathode was much improved due to the low surface energy of the InP nanopillars. A stable cathodic photocurrent of ca. 37 mA cm^{-2} can be achieved for at least four hours. Therefore, the nanostructuring of the planar InP photocathodes was found to drastically enhance its PEC performances due to the improved light absorbance and surface properties related to the desorption of the as-evolved H_2 gas.

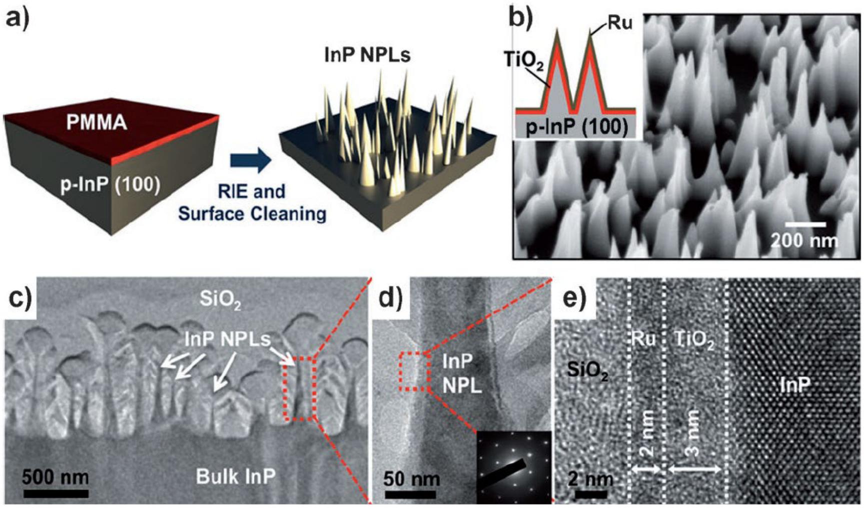

Figure 12. (**a**) Process flow for fabrication of InP nanopillar arrays. (**b**) SEM image of the resulting NPL arrays. Inset shows the schematic of a PEC cell made of p-InP NPLs, a TiO_2 passivation layer (thickness, 3–5 nm), and the Ru cocatalyst (thickness, ca. 2 nm). (**c**–**e**) TEM images of the p-InP NPLs coated with TiO_2/Ru layers. The inset in (**d**) shows diffraction patterns confirming the crystalline structure of InP NPLs. Reproduced with permission from [162]. Copyright WILEY-VCH Verlag GmbH & Co. KGaA, Weinheim, 2012.

2.6. Iodide-based Semiconductor Materials

2.6.1. BiOI

Bismuth oxyhalides, BiOX (X = Cl, Br, I), are a series of Bi-based semiconductor materials with varying band gaps related to the type of X. BiOI has the smallest band gap among these materials, with an indirect band gap typically between 1.7 and 1.9 eV. BiOI with different morphologies has been synthesized and extensively investigated [163–165]. Hahn et al. investigated the PEC properties of n-type BiOI photoanode for water splitting [166]. Their work employed a spray pyrolysis approach to preparing BiOI nanoplatelet film photoelectrodes on FTO substrates at different temperatures. The as-obtained BiOI films showed an n-type property, most likely due to the existence of anion vacancies. The BiOI film prepared at 533 K showed the optimum photocurrent of 0.9 mA cm^{-2} at 0.4 V vs. Ag/AgCl and IPCE of more than 20% in 0.25 M NaI acetonitrile solution due to the oxidation of I^- to I_3^-during the PEC reactions (Figure 13). The photons in the visible region ($\lambda > 420$ nm) contributed ca. 75% of the total photocurrent under AM 1.5G irradiation. However, the BiOI photoanode showed poor durability in aqueous solutions due to the oxidation of I^- in BiOI and the subsequent formation of an insulating bismuth hydroxide layer. It is anticipated that the modification of BiOI with a cocatalyst layer or the insulation of BiOI with a proper protection layer will lead to stable PEC water splitting, which has been observed in several semiconductor materials such as Cu_2O, WSe_2, and InP detailed in this review.

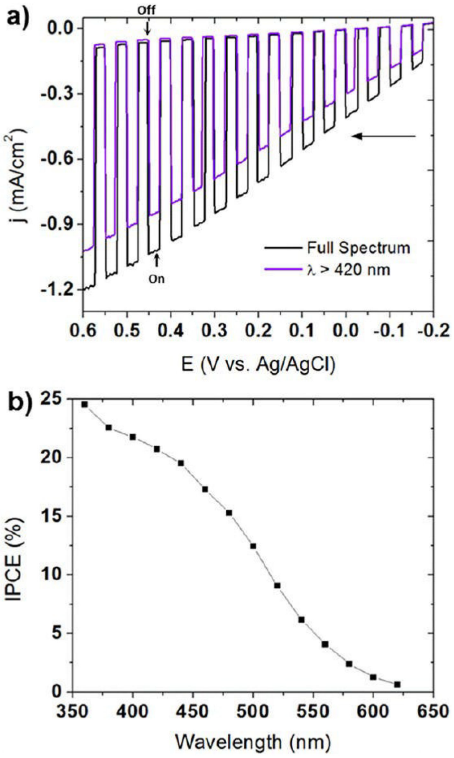

Figure 13. (**a**) Linear sweep voltammetry plot using a three-electrode configuration in 0.25 M NaI/acetonitrile with and without a 420 nm cut-on filter for an optimized BiOI film deposited at 533 K. The anodic scan rate was 25 mV s^{-1}. (**b**) IPCE spectrum recorded at 0.4 V vs. Ag/AgCl for a typical BiOI film deposited at 533 K with a peak light intensity of 476 µW cm^{-2}. Reproduced with permission from [166]. Copyright American Chemical Society, 2012.

2.6.2. $CH_3NH_3PbI_3$

Recently, halide perovskite materials have emerged as promising candidates for high-performance optoelectronic devices [167]. The general formula of halide perovskite materials is ABX_3, where A is usually $CH_3NH_3^+$ (MA), CH $(NH_2)_2^+$ (FA), or Cs^+, B is Pb^{2+} or Sn^{2+}, X is a halide anion (e.g., I^-, Br^-, Cl^-) [168]. The compositions of the halide perovskite materials determine their band gaps. Typically, the I-based perovskites have band gaps smaller than 2.1 eV, including $MAPbI_3$ (1.6 eV), $FAPbI_3$ (1.4 eV), and $CsPbI_3$ (1.8 eV), among others [169].

The halide perovskite materials were first discovered in 1978 [170]. However, the rapid development of these materials was encouraged by Miyasaka in 2009 [171]. Miyasaka et al. first employed $MAPbI_3$ in solar cells with a power conversion efficiency (PCE) of 3.8%. Then many efforts have been devoted to enhancing efficiency [172]. Up to now, the certified PCE has reached up to 25.7% [173]. The high PCEs of perovskite solar cells were ascribed to their excellent optoelectronic characteristics [174], including high light absorption coefficient, tunable band gap, and long charge carrier lifetime, which are also desirable properties for photocatalytic or PEC hydrogen evolution. However, due to the extreme susceptibility to water, halide perovskite materials are hindered from solar fuel production [175–177].

Nam et al. first used $MAPbI_3$ particles for photocatalytic hydrogen evolution in a saturated HI aqueous solution [178]. They found that $MAPbI_3$ powders can be stable in an aqueous solution when finely controlling the concentrations of H^+ and I^- due to the formation of a dynamic equilibrium between the dissolved species and the precipitate. Therefore, a photocatalytic HI splitting reaction was realized by $MAPbI_3$ particles to generate hydrogen. After the modification of Pt as a cocatalyst, the performance could be enhanced, and a solar-to-fuel conversion efficiency of 0.81% was achieved.

Other researchers have widely employed this dynamic equilibrium strategy [177]. For example, Huang and co-workers demonstrated that reduced graphene oxide (rGO) grafted on $MAPbI_3$ could act as an electron acceptor to significantly improve hydrogen evolution activity [179]. The photogenerated electrons from $MAPbI_3$ can, in situ, photoreduce graphene oxide to rGO, and then a composite of rGO and $MAPbI_3$ ($MAPbI_3$/rGO) was formed. The $MAPbI_3$/rGO showed 67 times enhancement in photocatalytic activity compared to bare $MAPbI_3$, ascribed to efficient extraction of photogenerated electrons from $MAPbI_3$ by rGO. Furthermore, the $MAPbI_3$/rGO showed good stability for photocatalytic hydrogen evolution with a continuous reaction of 200 h. Our group also reported that Pt/TiO_2 nanoparticles could drastically promote charge separation and transportation of $MAPbI_3$ particles (Figure 14) [180]. TiO_2 pre-deposited with Pt was introduced to $MAPbI_3$ particles to establish a dynamically-existing heterojunction, which enhanced photocatalytic activity. The rate of hydrogen evolution on Pt/TiO_2-$MAPbI_3$ was 89-fold higher than that of Pt/$MAPbI_3$. The solar-to-fuel conversion efficiency of Pt/TiO_2-$MAPbI_3$ was 0.86%. In addition, considering that Pt was a noble metal, substantial earth-abundant materials, such as Ni_3C, MoS_2, and CoP have been reported as alternative cocatalysts [181–184].

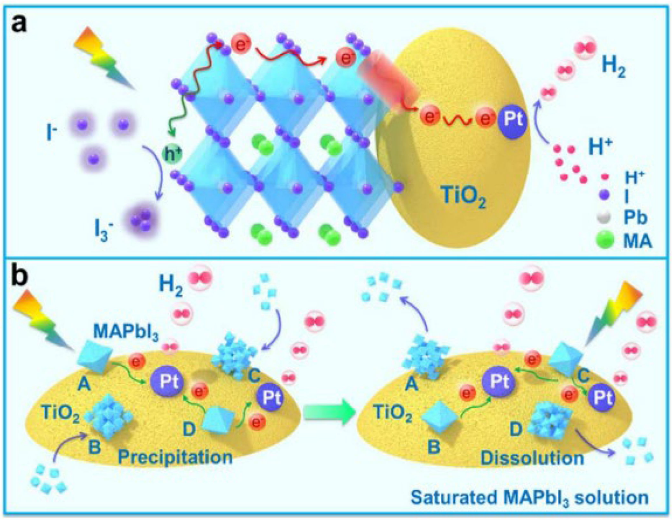

Figure 14. Schematic illustration of the photocatalytic H_2 evolution from HI splitting on Pt/TiO_2-$MAPbI_3$. (**a**) A nanoscale electron transporting channel was established between Pt/TiO_2 and $MAPbI_3$. (**b**) The dissolution and re-precipitation of $MAPbI_3$ in the saturated HI solution formed the dynamic interface between Pt/TiO_2 and $MAPbI_3$. Reproduced with permission from [180]. Copyright American Chemical Society, 2018.

Halide perovskite materials have also been investigated as photoelectrode materials for PEC water splitting. However, the inherent instability of halide perovskite materials in water hinders their application in PEC reactions. Therefore, many strategies have been developed to protect perovskite-based photoelectrodes. Zheng et al. first reported a Ni-protected $MAPbI_3$ photoanode [185]. A Ni layer deposited on the top of $MAPbI_3$ can improve the stability of PEC S^{2-} oxidation. The photoanode lost most of its activity after a 1000 s continuous reaction. Yang et al. used hydrophobic alkylammonium cations to functionalize $MAPbI_3$ photoanodes [186]. The stability of the photoanode was enhanced to 30 min. Other strategies, such as atomic layer deposited TiO_2 [187], carbon nanotube/polymer composite film encapsulation [188], and mesoporous carbon protection layer [189], were also employed to improve the stability of perovskite-based photoelectrodes. Up to now, one of the most effective strategies has been demonstrated by Reisner et al. [190]. They used a Field's metal (an alloy of In, Bi, and Sn) to encapsulate the $MAPbI_3$ photocathode. The Field's metal can well-protect $MAPbI_3$ to avoid the permeation of water while still efficiently transferring photogenerated electrons from the photocathode to the electrolyte. The photocathode showed a current density of -9.8 mA cm^{-2} at 0 V vs. RHE with enhanced durability of 1 h under continuous reaction. Following Reisner's strategy, many works have been reported [191–193]. Our group developed a Ti foil-encapsulated $MAPbI_3$ photocathode with a sandwich-like structure [194]. As a hydrogen evolution cocatalyst, Pt was pre-deposited on the Ti foil using the magnetron sputtering method. The sandwich-like photocathode displayed a current density of -18 mA cm^{-2} at 0 V vs. RHE. Moreover, it showed excellent stability under 12 h of continuous reaction in water. This work paves the way for employing halide perovskite materials in solar fuel production.

2.7. Silicon and Silicide-Based Semiconductor Materials

2.7.1. Si

Si (Silicon) has a band gap of 1.12 eV and can utilize solar energy of up to 1000 nm. The conduction band edge of Si is high enough to reduce water to H_2, while an external power source is needed to drive overall water splitting. Si has been commercially used in the photovoltaic industry as an earth-abundant semiconductor material. Due to the great potential for the fabrication of efficient photoelectrode for PEC water splitting, Si has been extensively investigated as the building block material for photoelectrode [195,196].

One problem of a planar Si-based film is that ca. 25% of incident light is reflected away from the Si surface, which limits the collection of the incident photons. Lewis and Atwater et al. reported the preparation of an efficient p-type silicon (p-Si) wire array on p^+-Si (111) substrates from $SiCl_4$ and BCl_3 precursors using a copper-catalyzed, vapor-liquid-solid-growth process. Energy conversion efficiencies of up to 3% and internal quantum yields of at least 0.7 were observed for these wire arrays in contact with an aqueous methyl vilolgen$^{2+/+}$ electrolyte during PEC water splitting [197]. They showed that compared with planar-sheet absorbers, Si wire arrays have beneficial optical features for photovoltaic applications, such as reasonable absorption of sunlight despite low areal packing fractions, enhanced near-infrared absorption, and effective optical concentration over a wide range of incidence angles [198]. These properties may be useful in improving the efficiency of the Si photoelectrode or reducing the material consumption for PEC water-splitting applications. In the following work, a radial n^+ emitter shell was formed on the surface of B-doped p-Si microwires, followed by the deposition of 1.5-nm-thick Pt film [199]. The as-prepared electrode yielded energy conversion efficiency >5% under one sun solar simulation in 0.5 M K_2SO_4 (pH = 2) solution, which is much higher than that of the analogous p-Si wire-array electrodes (<0.2%). The higher photovoltage generated at the n^+ p-Si/H_2O junction is supposed to be the main reason for its higher PEC performance. Oh et al. prepared a nanoporous black silicon photocathode with a simple single-step metal-assisted etching technique [200]. Compared with traditional planar silicon photoelectrode, the nanoporous photoelectrode has several advantages, such as broadband anti-reflection that enables efficient absorption of the incident light, higher effective surface reactions sites in contact with water, lower overpotential required to drive PEC water reduction, and less need for surfactant in the electrolyte to promote H_2 evolution. Similarly, the Si nanowire array photocathode was fabricated by metal-catalyzed electroless etching, which demonstrated superior PEC performance than the planar Si photoelectrode [201].

The problem for Si is its instability during long-term PEC water reactions, which is especially serious for n-type Si photoanodes under anodic conditions. Therefore, different strategies have been developed to improve the stability of Si electrodes [202]. The common way to improve the stability of Si electrodes is to deposit a charge tunneling layer or catalytic layer on the Si surface to avoid the direct contact of Si with an aqueous solution or promote a water catalysis reaction. Chen et al. reported the deposition of a protective 2 nm thick TiO_2 layer with the atomic layer deposition method on Si photoanode followed by coating with a 3 nm iridium catalyst layer. The as-prepared photoanode exhibited sustained water oxidation capability for many hours under harsh pH and oxidative conditions, while silicon photoanodes without the TiO_2 layer quickly failed [203]. Brian et al. sputtered a thin layer of Ti on the n^+ p-Si photocathode, followed by the deposition of a molybdenum sulfide catalyst. The Ti layer can protect the photoelectrode from oxidation, and molybdenum sulfide can work as a substitute for Pt to promote water reduction performance [204]. Other strategies, such as the coating of the metal oxide protective layer, Ni-Mo, and CoPi catalyst, have demonstrated their capacity for enhancing the PEC performance of Si-based photoelectrode [205–214].

2.7.2. $TiSi_2$

Ritterskamp et al. reported the photocatalytic water splitting on commercial titanium disilicide ($TiSi_2$) derived semiconducting catalyst under solar radiation [215,216]. Different from the classical semiconductor materials, which exhibit small band gap spreads, the dark grey $TiSi_2$ can absorb light within a wide range of 360 to 800 nm. The Fermi level of $TiSi_2$ was measured to be located at −0.43 eV and −0.41 eV before and during the reaction at pH = 7, respectively. Therefore, the energy level is high enough to fulfill the thermodynamic requirement for the proton reduction reactions. Under solar light irradiation, two phases (A and B) of H_2 evolution from pure water were observed when $TiSi_2$ power was allowed to react under standard conditions. As shown in Figure 15, H_2 evolution due to the surface passivation and photocatalytic water splitting occurred in phase A, during which the catalytic centers for water oxidation and proton reduction were in situ generated. In phase B, H_2 production from the photocatalytic process contributed to more than 96% of the total H_2 produced. One interesting finding for the $TiSi_2$ catalyst is that O_2 can store in the $TiSi_2$ catalyst and can be liberated upon heating to 373 K. Therefore, $TiSi_2$ is a unique photocatalyst with the capability of self-separating H_2 and O_2 products from water splitting under solar irradiation.

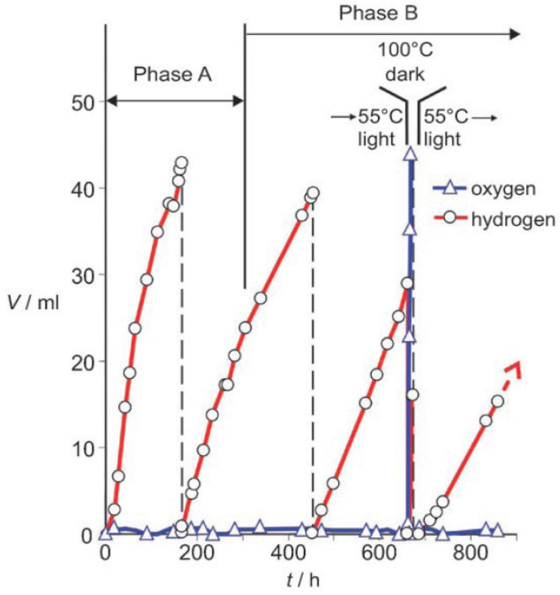

Figure 15. The representative reaction of $TiSi_2$ at 328 K under standard conditions. Reproduced with permission from [215]. Copyright WILEY-VCH Verlag GmbH & Co. KGaA, Weinheim, 2007.

Banerjee et al. investigated the PEC performance of a photoanode composed of $TiSi_2$ nanoparticles that were assembled onto a TiO_2 nanotube array [217]. The TiO_2 nanotube array was synthesized using a sonoelectrochemical anodization method. $TiSi_2$ nanoparticles were prepared by ball milling commercial $TiSi_2$ particles followed by ultrasonication processing. The $TiSi_2$ nanoparticles were then assembled onto the TiO_2 nanotube array using the multiple impregnation method. The resulting $TiSi_2$-TiO_2 heterostructural composite photoanode showed a photocurrent of 3.49 mA/cm^2 at 1.2 V vs. NHE under AM 1.5G irradiation conditions, while only photocurrents of 0.9 mA/cm^2 and 0.26 mA/cm^2 were achieved on TiO_2 nanotubes or $TiSi_2$ photoelectrodes alone at the same conditions. The enhanced solar light absorption of $TiSi_2$ and increased charge transport abilities of one-dimensional TiO_2 NTs are supposed to be responsible for the excellent photoactivity of this hybrid photoanode.

3. Conclusions and Prospects

The development of small band gap semiconductor materials with suitable energy levels is crucial for efficient solar H_2 production from PEC or photocatalytic water splitting. Significant efforts have been devoted to exploring and modifying visible-light-responsive semiconductor materials, and several important signs of progress have been witnessed. For example, various material systems have demonstrated the capability for overall photocatalytic water splitting under visible light, which has been supposed to be one of the "Holy Grails" of chemistry. Although this proof-of-concept evidence is encouraging, no photocatalytic water splitting system can achieve solar energy conversion efficiency of more than 10%, even though different strategies have been proposed to improve photocatalytic performance. This is partially due to the extremely stringent thermodynamic requirement on the materials themselves and the unavoidable severe recombination of photogenerated charges. On the other hand, several small band gap semiconductor material systems have shown appreciable energy conversion efficiency of more than 10% for PEC water splitting under applied bias. Even though these efficient PEC devices could be used in some special conditions, the expensive material supply and the high fabrication cost will limit their wide application. In order to achieve a PEC system that can be met with the economic feasibility for practical solar H_2 production, developing small band gap ($\leq$2.1 eV), cost-effective, environmentally benign, and stable semiconductor materials should be the future research focus. It is worth noting that computational models and theoretical simulations can investigate the materials' band structures and electronic states, which could help us rationally synthesize semiconductors. Moreover, high-throughput computational screening efficiently identifies potential candidates for photocatalytic and PEC hydrogen evolution. The combination of experimental and theoretical results will facilitate the development of semiconductor materials for solar water splitting.

Author Contributions: Conceptualization, X.Z.; Investigation and data analysis, H.Z.; visualization, J.L. and T.X.; resources, W.J.; funding acquisition, H.Z.; writing—original draft preparation, H.Z. and X.Z.; writing—review and editing, H.Z. and X.Z. All authors have read and agreed to the published version of the manuscript.

Funding: This work was funded by the China Postdoctoral Science Foundation (grant number 2021M700651) and the Fundamental Research Funds for the Central Universities (grant numbers 3132022216 and 3132022217).

Data Availability Statement: Not applicable.

Conflicts of Interest: The authors declare no conflict of interest.

References

1. Navarro, R.M.; Alvarez-Galván, M.C.; Villoria de la Mano, J.A.; Al-Zahrani, S.M.; Fierro, J.L.G. A framework for visible-light water splitting. *Energy Environ. Sci.* **2010**, *3*, 1865–1882. [CrossRef]
2. Linsebigler, A.L.; Lu, G.; Yates, J.T., Jr. Photocatalysis on TiO_2 Surfaces: Principles, Mechanisms, and Selected Results. *Chem. Rev.* **1995**, *95*, 735–758. [CrossRef]
3. Bard, A.J.; Fox, M.A. Artificial Photosynthesis: Solar Splitting of Water to Hydrogen and Oxygen. *Acc. Chem. Res.* **1995**, *28*, 141–145. [CrossRef]
4. Armaroli, N.; Balzani, V. The Future of Energy Supply: Challenges and Opportunities. *Angew. Chem. Int. Ed.* **2007**, *46*, 52–66. [CrossRef] [PubMed]
5. Wang, Z.; Hisatomi, T.; Li, R.; Sayama, K.; Liu, G.; Domen, K.; Li, C.; Wang, L. Efficiency Accreditation and Testing Protocols for Particulate Photocatalysts toward Solar Fuel Production. *Joule* **2021**, *5*, 344–359. [CrossRef]
6. Fujishima, A.; Honda, K. Electrochemical Photolysis of Water at a Semiconductor Electrode. *Nature* **1972**, *238*, 37–38. [CrossRef]
7. Abe, R. Recent progress on photocatalytic and photoelectrochemical water splitting under visible light irradiation. *J. Photochem. Photobiol. C-Photochem. Rev.* **2010**, *11*, 179–209. [CrossRef]

8. Chen, Z.; Jaramillo, T.F.; Deutsch, T.G.; Kleiman-Shwarsctein, A.; Forman, A.J.; Gaillard, N.; Garland, R.; Takanabe, K.; Heske, C.; Sunkara, M.; et al. Accelerating materials development for photoelectrochemical hydrogen production: Standards for methods, definitions, and reporting protocols. *J. Mater. Res.* **2011**, *25*, 3–16. [CrossRef]
9. Service, R.F. Catalyst Boosts Hopes for Hydrogen Bonanza. *Science* **2002**, *297*, 2189–2190. [CrossRef] [PubMed]
10. Chen, X.; Shen, S.; Guo, L.; Mao, S.S. Semiconductor-based Photocatalytic Hydrogen Generation. *Chem. Rev.* **2010**, *110*, 6503–6570. [CrossRef]
11. Ma, Y.; Wang, X.; Jia, Y.; Chen, X.; Han, H.; Li, C. Titanium Dioxide-Based Nanomaterials for Photocatalytic Fuel Generations. *Chem. Rev.* **2014**, *114*, 9987–10043. [CrossRef] [PubMed]
12. Tao, X.; Zhao, Y.; Wang, S.; Li, C.; Li, R. Recent advances and perspectives for solar-driven water splitting using particulate photocatalysts. *Chem. Soc. Rev.* **2022**, *51*, 3561–3608. [CrossRef] [PubMed]
13. Walter, M.G.; Warren, E.L.; McKone, J.R.; Boettcher, S.W.; Mi, Q.; Santori, E.A.; Lewis, N.S. Solar Water Splitting Cells. *Chem. Rev.* **2010**, *110*, 6446–6473. [CrossRef] [PubMed]
14. Li, Z.; Luo, W.; Zhang, M.; Feng, J.; Zou, Z. Photoelectrochemical cells for solar hydrogen production: Current state of promising photoelectrodes, methods to improve their properties, and outlook. *Energy Environ. Sci.* **2013**, *6*, 347–370. [CrossRef]
15. Kim, J.H.; Hansora, D.; Sharma, P.; Jang, J.-W.; Lee, J.S. Toward practical solar hydrogen production—An artificial photosynthetic leaf-to-farm challenge. *Chem. Soc. Rev.* **2019**, *48*, 1908–1971. [CrossRef]
16. Hisatomi, T.; Kubota, J.; Domen, K. Recent advances in semiconductors for photocatalytic and photoelectrochemical water splitting. *Chem. Soc. Rev.* **2014**, *43*, 7520–7535. [CrossRef]
17. Maeda, K.; Domen, K. Photocatalytic Water Splitting: Recent Progress and Future Challenges. *J. Phys. Chem. Lett.* **2010**, *1*, 2655–2661. [CrossRef]
18. Hernández-Alonso, M.D.; Fresno, F.; Suárez, S.; Coronado, J.M. Development of alternative photocatalysts to TiO_2: Challenges and opportunities. *Energy Environ. Sci.* **2009**, *2*, 1231–1257. [CrossRef]
19. Navarro, R.M.; Sánchez-Sánchez, M.C.; Alvarez-Galvan, M.C.; Valle, F.d.; Fierro, J.L.G. Hydrogen production from renewable sources: Biomass and photocatalytic opportunities. *Energy Environ. Sci.* **2009**, *2*, 35–54. [CrossRef]
20. Shimura, K.; Yoshida, H. Heterogeneous photocatalytic hydrogen production from water and biomass derivatives. *Energy Environ. Sci.* **2011**, *4*, 2467–2481. [CrossRef]
21. Osterloh, F.E. Inorganic Materials as Catalysts for Photochemical Splitting of Water. *Chem. Mater.* **2008**, *20*, 35–54. [CrossRef]
22. Tong, H.; Ouyang, S.; Bi, Y.; Umezawa, N.; Oshikiri, M.; Ye, J. Nano-photocatalytic Materials: Possibilities and Challenges. *Adv. Mater.* **2012**, *24*, 229–251. [CrossRef] [PubMed]
23. Kudo, A. Development of photocatalyst materials for water splitting. *Int. J. Hydrogen Energy* **2006**, *31*, 197–202. [CrossRef]
24. Takata, T.; Jiang, J.; Sakata, Y.; Nakabayashi, M.; Shibata, N.; Nandal, V.; Seki, K.; Hisatomi, T.; Domen, K. Photocatalytic water splitting with a quantum efficiency of almost unity. *Nature* **2020**, *581*, 411–414. [CrossRef]
25. Wang, Q.; Pornrungroj, C.; Linley, S.; Reisner, E. Strategies to improve light utilization in solar fuel synthesis. *Nat. Energy* **2022**, *7*, 13–24. [CrossRef]
26. Wang, Q.; Hisatomi, T.; Jia, Q.; Tokudome, H.; Zhong, M.; Wang, C.; Pan, Z.; Takata, T.; Nakabayashi, M.; Shibata, N.; et al. Scalable water splitting on particulate photocatalyst sheets with a solar-to-hydrogen energy conversion efficiency exceeding 1%. *Nat. Mater.* **2016**, *15*, 611–615. [CrossRef]
27. Pan, L.; Kim, J.H.; Mayer, M.T.; Son, M.-K.; Ummadisingu, A.; Lee, J.S.; Hagfeldt, A.; Luo, J.; Grätzel, M. Boosting the performance of Cu2O photocathodes for unassisted solar water splitting devices. *Nat. Catal.* **2018**, *1*, 412–420. [CrossRef]
28. Zhou, P.; Navid, I.A.; Ma, Y.; Xiao, Y.; Wang, P.; Ye, Z.; Zhou, B.; Sun, K.; Mi, Z. Solar-to-hydrogen efficiency of more than 9% in photocatalytic water splitting. *Nature* **2023**, *613*, 66–70. [CrossRef] [PubMed]
29. Kobayashi, H.; Sato, N.; Orita, M.; Kuang, Y.; Kaneko, H.; Minegishi, T.; Yamada, T.; Domen, K. Development of highly efficient $CuIn_{0.5}Ga_{0.5}Se_2$-based photocathode and application to overall solar driven water splitting. *Energy Environ. Sci.* **2018**, *11*, 3003–3009. [CrossRef]
30. Cheng, W.-H.; Richter, M.H.; May, M.M.; Ohlmann, J.; Lackner, D.; Dimroth, F.; Hannappel, T.; Atwater, H.A.; Lewerenz, H.-J. Monolithic Photoelectrochemical Device for Direct Water Splitting with 19% Efficiency. *ACS Energy Lett.* **2018**, *3*, 1795–1800. [CrossRef]
31. Higashi, T.; Nishiyama, H.; Suzuki, Y.; Sasaki, Y.; Hisatomi, T.; Katayama, M.; Minegishi, T.; Seki, K.; Yamada, T.; Domen, K. Transparent Ta_3N_5 Photoanodes for Efficient Oxygen Evolution toward the Development of Tandem Cells. *Angew. Chem. Int. Ed.* **2019**, *58*, 2300–2304. [CrossRef]
32. Jafari, T.; Moharreri, E.; Amin, A.S.; Miao, R.; Song, W.; Suib, S.L. Photocatalytic Water Splitting—The Untamed Dream: A Review of Recent Advances. *Molecules* **2016**, *21*, 900. [CrossRef] [PubMed]
33. Zhao, C.; Chen, Z.; Shi, R.; Yang, X.; Zhang, T. Recent Advances in Conjugated Polymers for Visible-Light-Driven Water Splitting. *Adv. Mater.* **2020**, *32*, 1907296. [CrossRef] [PubMed]
34. Zhang, G.; Lan, Z.-A.; Wang, X. Conjugated Polymers: Catalysts for Photocatalytic Hydrogen Evolution. *Angew. Chem. Int. Ed.* **2016**, *55*, 15712–15727. [CrossRef]
35. Rahman, M.; Tian, H.; Edvinsson, T. Revisiting the Limiting Factors for Overall Water-Splitting on Organic Photocatalysts. *Angew. Chem. Int. Ed.* **2020**, *59*, 16278–16293. [CrossRef]

36. Sun, R.; Tan, B. Covalent Triazine Frameworks (CTFs): Synthesis, Crystallization, and Photocatalytic Water Splitting. *Chem. Eur. J.* **2023**, *29*, e202203077.
37. Kudo, A.; Miseki, Y. Heterogeneous photocatalyst materials for water splitting. *Chem. Soc. Rev.* **2009**, *38*, 253–278. [CrossRef] [PubMed]
38. Vesborg, P.C.K.; Jaramillo, T.F. Addressing the terawatt challenge: Scalability in the supply of chemical elements for renewable energy. *RSC Adv.* **2012**, *2*, 7933–7947. [CrossRef]
39. Glasscock, J.A.; Barnes, P.R.F.; Plumb, I.C.; Bendavid, A.; Martin, P.J. Structural, optical and electrical properties of undoped polycrystalline hematite thin films produced using filtered arc deposition. *Thin Solid Films* **2008**, *516*, 1716–1724. [CrossRef]
40. Cherepy, N.J.; Liston, D.B.; Lovejoy, J.A.; Deng, H.; Zhang, J.Z. Ultrafast Studies of Photoexcited Electron Dynamics in γ- and α-Fe_2O_3 Semiconductor Nanoparticles. *J. Phys. Chem. B* **1998**, *102*, 770–776. [CrossRef]
41. Ling, Y.; Wang, G.; Wheeler, D.A.; Zhang, J.Z.; Li, Y. Sn-Doped Hematite Nanostructures for Photoelectrochemical Water Splitting. *Nano Lett.* **2011**, *11*, 2119–2125. [CrossRef]
42. Lin, Y.; Zhou, S.; Sheehan, S.W.; Wang, D. Nanonet-Based Hematite Heteronanostructures for Efficient Solar Water Splitting. *J. Am. Chem. Soc.* **2011**, *133*, 2398–2401. [CrossRef] [PubMed]
43. Franking, R.; Li, L.; Lukowski, M.A.; Meng, F.; Tan, Y.; Hamers, R.J.; Jin, S. Facile post-growth doping of nanostructured hematite photoanodes for enhanced photoelectrochemical water oxidation. *Energy Environ. Sci.* **2013**, *6*, 500–512. [CrossRef]
44. Sivula, K.; Zboril, R.; Le Formal, F.; Robert, R.; Weidenkaff, A.; Tucek, J.; Frydrych, J.; Grätzel, M. Photoelectrochemical Water Splitting with Mesoporous Hematite Prepared by a Solution-Based Colloidal Approach. *J. Am. Chem. Soc.* **2010**, *132*, 7436–7444. [CrossRef]
45. Zhong, D.K.; Gamelin, D.R. Photoelectrochemical Water Oxidation by Cobalt Catalyst (“Co−Pi”)/α-Fe_2O_3 Composite Photoanodes: Oxygen Evolution and Resolution of a Kinetic Bottleneck. *J. Am. Chem. Soc.* **2010**, *132*, 4202–4207. [CrossRef]
46. Joya, K.S.; Morlanés, N.; Maloney, E.; Rodionov, V.; Takanabe, K. Immobilization of a molecular cobalt electrocatalyst by hydrophobic interaction with a hematite photoanode for highly stable oxygen evolution. *Chem. Commun.* **2015**, *51*, 13481–13484. [CrossRef]
47. Dhandole, L.K.; Koh, T.S.; Anushkkaran, P.; Chung, H.-S.; Chae, W.-S.; Lee, H.H.; Choi, S.H.; Cho, M.; Jang, J.S. Enhanced charge transfer with tuning surface state in hematite photoanode integrated by niobium and zirconium co-doping for efficient photoelectrochemical water splitting. *Appl. Catal. B Environ.* **2022**, *315*, 121538. [CrossRef]
48. Ahmed, A.Y.; Ahmed, M.G.; Kandiel, T.A. Modification of Hematite Photoanode with Cobalt Based Oxygen Evolution Catalyst via Bifunctional Linker Approach for Efficient Water Splitting. *J. Phys. Chem. C* **2016**, *120*, 23415–23420. [CrossRef]
49. Wu, Q.; Meng, D.; Zhang, Y.; Zhao, Q.; Bu, Q.; Wang, D.; Zou, X.; Lin, Y.; Li, S.; Xie, T. Acid-treated Ti^{4+} doped hematite photoanode for efficient solar water oxidation—Insight into surface states and charge separation. *J. Alloys Compd.* **2019**, *782*, 943–951. [CrossRef]
50. Jiang, D.; Yue, Q.; Tang, S.; Zhang, L.; Zhu, L.; Du, P. A highly efficient photoelectrochemical cell using cobalt phosphide-modified nanoporous hematite photoanode for solar-driven water splitting. *J. Catal.* **2018**, *366*, 275–281. [CrossRef]
51. Wang, Z.; Mao, X.; Chen, P.; Xiao, M.; Monny, S.A.; Wang, S.; Konarova, M.; Du, A.; Wang, L. Understanding the Roles of Oxygen Vacancies in Hematite-Based Photoelectrochemical Processes. *Angew. Chem. Int. Ed.* **2019**, *58*, 1030–1034. [CrossRef]
52. Wheeler, D.A.; Wang, G.; Ling, Y.; Li, Y.; Zhang, J.Z. Nanostructured hematite: Synthesis, characterization, charge carrier dynamics, and photoelectrochemical properties. *Energy Environ. Sci.* **2012**, *5*, 6682–6702. [CrossRef]
53. Shen, S.; Lindley, S.A.; Chen, X.; Zhang, J.Z. Hematite heterostructures for photoelectrochemical water splitting: Rational materials design and charge carrier dynamics. *Energy Environ. Sci.* **2016**, *9*, 2744–2775. [CrossRef]
54. Kment, S.; Riboni, F.; Pausova, S.; Wang, L.; Wang, L.; Han, H.; Hubicka, Z.; Krysa, J.; Schmuki, P.; Zboril, R. Photoanodes based on TiO_2 and α-Fe_2O_3 for solar water splitting—superior role of 1D nanoarchitectures and of combined heterostructures. *Chem. Soc. Rev.* **2017**, *46*, 3716–3769. [CrossRef]
55. Li, J.; Chen, H.; Triana, C.A.; Patzke, G.R. Hematite Photoanodes for Water Oxidation: Electronic Transitions, Carrier Dynamics, and Surface Energetics. *Angew. Chem. Int. Ed.* **2021**, *60*, 18380–18396. [CrossRef]
56. Bedin, K.C.; Muche, D.N.F.; Melo, M.A., Jr.; Freitas, A.L.M.; Gonçalves, R.V.; Souza, F.L. Role of Cocatalysts on Hematite Photoanodes in Photoelectrocatalytic Water Splitting: Challenges and Future Perspectives. *ChemCatChem* **2020**, *12*, 3156–3169. [CrossRef]
57. Lv, X.; Zhang, G.; Wang, M.; Li, G.; Deng, J.; Zhong, J. How titanium and iron are integrated into hematite to enhance the photoelectrochemical water oxidation: A review. *Phys. Chem. Chem. Phys.* **2023**, *25*, 1406–1420. [CrossRef] [PubMed]
58. Iandolo, B.; Wickman, B.; Zorić, I.; Hellman, A. The rise of hematite: Origin and strategies to reduce the high onset potential for the oxygen evolution reaction. *J. Mater. Chem. A* **2015**, *3*, 16896–16912. [CrossRef]
59. Tilley, S.D.; Cornuz, M.; Sivula, K.; Grätzel, M. Light-Induced Water Splitting with Hematite: Improved Nanostructure and Iridium Oxide Catalysis. *Angew. Chem. Int. Ed.* **2010**, *49*, 6405–6408. [CrossRef]
60. Kay, A.; Cesar, I.; Grätzel, M. New Benchmark for Water Photooxidation by Nanostructured α-Fe_2O_3 Films. *J. Am. Chem. Soc.* **2006**, *128*, 15714–15721. [CrossRef] [PubMed]
61. Zhong, D.K.; Sun, J.; Inumaru, H.; Gamelin, D.R. Solar Water Oxidation by Composite Catalyst/α-Fe_2O_3 Photoanodes. *J. Am. Chem. Soc.* **2009**, *131*, 6086–6087. [CrossRef] [PubMed]

62. Barroso, M.; Cowan, A.J.; Pendlebury, S.R.; Grätzel, M.; Klug, D.R.; Durrant, J.R. The Role of Cobalt Phosphate in Enhancing the Photocatalytic Activity of α-Fe_2O_3 toward Water Oxidation. *J. Am. Chem. Soc.* **2011**, *133*, 14868–14871. [CrossRef] [PubMed]
63. Brillet, J.; Grätzel, M.; Sivula, K. Decoupling Feature Size and Functionality in Solution-Processed, Porous Hematite Electrodes for Solar Water Splitting. *Nano Lett.* **2010**, *10*, 4155–4160. [CrossRef]
64. Hisatomi, T.; Le Formal, F.; Cornuz, M.; Brillet, J.; Tétreault, N.; Sivula, K.; Grätzel, M. Cathodic shift in onset potential of solar oxygen evolution on hematite by 13-group oxide overlayers. *Energy Environ. Sci.* **2011**, *4*, 2512–2515. [CrossRef]
65. Wang, G.; Ling, Y.; Wheeler, D.A.; George, K.E.N.; Horsley, K.; Heske, C.; Zhang, J.Z.; Li, Y. Facile Synthesis of Highly Photoactive α-Fe_2O_3-Based Films for Water Oxidation. *Nano Lett.* **2011**, *11*, 3503–3509. [CrossRef]
66. Ling, Y.; Wang, G.; Reddy, J.; Wang, C.; Zhang, J.Z.; Li, Y. The Influence of Oxygen Content on the Thermal Activation of Hematite Nanowires. *Angew. Chem. Int. Ed.* **2012**, *51*, 4074–4079. [CrossRef]
67. Bagal, I.V.; Chodankar, N.R.; Hassan, M.A.; Waseem, A.; Johar, M.A.; Kim, D.-H.; Ryu, S.-W. Cu_2O as an emerging photocathode for solar water splitting—A status review. *Int. J. Hydrogen Energy* **2019**, *44*, 21351–21378. [CrossRef]
68. Lumley, M.A.; Radmilovic, A.; Jang, Y.J.; Lindberg, A.E.; Choi, K.-S. Perspectives on the Development of Oxide-Based Photocathodes for Solar Fuel Production. *J. Am. Chem. Soc.* **2019**, *141*, 18358–18369. [CrossRef] [PubMed]
69. Li, S.; Mo, Q.-L.; Xiao, Y.; Xiao, F.-X. Maneuvering cuprous oxide-based photocathodes for solar-to-fuel conversion. *Coord. Chem. Rev.* **2023**, *477*, 214948. [CrossRef]
70. Nishikawa, M.; Fukuda, M.; Nakabayashi, Y.; Saito, N.; Ogawa, N.; Nakajima, T.; Shinoda, K.; Tsuchiya, T.; Nosaka, Y. A method to give chemically stabilities of photoelectrodes for water splitting: Compositing of a highly crystalized TiO_2 layer on a chemically unstable Cu_2O photocathode using laser-induced crystallization process. *Appl. Surf. Sci.* **2016**, *363*, 173–180. [CrossRef]
71. Dubale, A.A.; Pan, C.-J.; Tamirat, A.G.; Chen, H.-M.; Su, W.-N.; Chen, C.-H.; Rick, J.; Ayele, D.W.; Aragaw, B.A.; Lee, J.-F.; et al. Heterostructured Cu_2O/CuO decorated with nickel as a highly efficient photocathode for photoelectrochemical water reduction. *J. Mater. Chem. A* **2015**, *3*, 12482–12499. [CrossRef]
72. Shi, W.; Zhang, X.; Li, S.; Zhang, B.; Wang, M.; Shen, Y. Carbon coated Cu_2O nanowires for photo-electrochemical water splitting with enhanced activity. *Appl. Surf. Sci.* **2015**, *358*, 404–411. [CrossRef]
73. Sun, H.; Dong, C.; Liu, Q.; Yuan, Y.; Zhang, T.; Zhang, J.; Hou, Y.; Zhang, D.; Feng, X. Conjugated Acetylenic Polymers Grafted Cuprous Oxide as an Efficient Z-Scheme Heterojunction for Photoelectrochemical Water Reduction. *Adv. Mater.* **2020**, *32*, 2002486. [CrossRef] [PubMed]
74. Li, C.; Hisatomi, T.; Watanabe, O.; Nakabayashi, M.; Shibata, N.; Domen, K.; Delaunay, J.-J. Positive onset potential and stability of Cu_2O-based photocathodes in water splitting by atomic layer deposition of a Ga_2O_3 buffer layer. *Energy Environ. Sci.* **2015**, *8*, 1493–1500. [CrossRef]
75. Paracchino, A.; Laporte, V.; Sivula, K.; Grätzel, M.; Thimsen, E. Highly active oxide photocathode for photoelectrochemical water reduction. *Nat. Mater.* **2011**, *10*, 456–461. [CrossRef]
76. Paracchino, A.; Mathews, N.; Hisatomi, T.; Stefik, M.; Tilley, S.D.; Grätzel, M. Ultrathin films on copper(i) oxide water splitting photocathodes: A study on performance and stability. *Energy Environ. Sci.* **2012**, *5*, 8673–8681. [CrossRef]
77. Zhang, Z.; Dua, R.; Zhang, L.; Zhu, H.; Zhang, H.; Wang, P. Carbon-Layer-Protected Cuprous Oxide Nanowire Arrays for Efficient Water Reduction. *ACS Nano* **2013**, *7*, 1709–1717. [CrossRef]
78. Lin, C.-Y.; Lai, Y.-H.; Mersch, D.; Reisner, E. $Cu_2O|NiO_x$ nanocomposite as an inexpensive photocathode in photoelectrochemical water splitting. *Chem. Sci.* **2012**, *3*, 3482–3487. [CrossRef]
79. Joshi, U.A.; Palasyuk, A.M.; Maggard, P.A. Photoelectrochemical Investigation and Electronic Structure of a p-Type $CuNbO_3$ Photocathode. *J. Phys. Chem. C* **2011**, *115*, 13534–13539. [CrossRef]
80. Joshi, U.A.; Maggard, P.A. $CuNb_3O_8$: A p-Type Semiconducting Metal Oxide Photoelectrode. *J. Phys. Chem. Lett.* **2012**, *3*, 1577–1581. [CrossRef]
81. Joshi, U.A.; Palasyuk, A.; Arney, D.; Maggard, P.A. Semiconducting Oxides to Facilitate the Conversion of Solar Energy to Chemical Fuels. *J. Phys. Chem. Lett.* **2010**, *1*, 2719–2726. [CrossRef]
82. Maggard, P.A. Capturing Metastable Oxide Semiconductors for Applications in Solar Energy Conversion. *Acc. Chem. Res.* **2021**, *54*, 3160–3171. [CrossRef]
83. Yamaguchi, A.; Sako, H.; Miyauchi, M. Synthesis of $CaFe_2O_4$ Nanorod Thin Film Using Molten Salt Method and Analysis of Its Photoelectrochemical Properties. *Chem. Lett.* **2020**, *49*, 1462–1464. [CrossRef]
84. Kirchberg, K.; Marschall, R. Sol–gel synthesis of mesoporous $CaFe_2O_4$ photocathodes with hierarchical pore morphology. *Sustain. Energy Fuels* **2019**, *3*, 1150–1153. [CrossRef]
85. Díez-García, M.I.; Gómez, R. Investigating Water Splitting with $CaFe_2O_4$ Photocathodes by Electrochemical Impedance Spectroscopy. *ACS Appl. Mater. Interfaces* **2016**, *8*, 21387–21397. [CrossRef]
86. Ida, S.; Yamada, K.; Matsunaga, T.; Hagiwara, H.; Matsumoto, Y.; Ishihara, T. Preparation of p-Type $CaFe_2O_4$ Photocathodes for Producing Hydrogen from Water. *J. Am. Chem. Soc.* **2010**, *132*, 17343–17345. [CrossRef] [PubMed]
87. Cao, J.; Kako, T.; Li, P.; Ouyang, S.; Ye, J. Fabrication of p-type $CaFe_2O_4$ nanofilms for photoelectrochemical hydrogen generation. *Electrochem. Commun.* **2011**, *13*, 275–278. [CrossRef]
88. Xu, X.; Randorn, C.; Efstathiou, P.; Irvine, J.T.S. A red metallic oxide photocatalyst. *Nat. Mater.* **2012**, *11*, 595–598. [CrossRef]
89. Go, H.; Akio, I.; Tsuyoshi, T.; Kondo, J.N.; Michikazu, H.; Kazunari, D. Ta_3N_5 as a Novel Visible Light-Driven Photocatalyst ($\lambda < 600$ nm). *Chem. Lett.* **2002**, *31*, 736–737.

90. Hara, M.; Hitoki, G.; Takata, T.; Kondo, J.N.; Kobayashi, H.; Domen, K. TaON and Ta_3N_5 as new visible light driven photocatalysts. *Catal. Today* **2003**, *78*, 555–560. [CrossRef]
91. Zhang, P.; Zhang, J.; Gong, J. Tantalum-based semiconductors for solar water splitting. *Chem. Soc. Rev.* **2014**, *43*, 4395–4422. [CrossRef]
92. Seo, J.; Nishiyama, H.; Yamada, T.; Domen, K. Visible-Light-Responsive Photoanodes for Highly Active, Stable Water Oxidation. *Angew. Chem. Int. Ed.* **2018**, *57*, 8396–8415. [CrossRef] [PubMed]
93. Yungi, L.; Kota, N.; Tomoaki, W.; Tsuyoshi, T.; Michikazu, H.; Masahiro, Y.; Kazunari, D. Effect of 10 MPa Ammonia Treatment on the Activity of Visible Light Responsive Ta_3N_5 Photocatalyst. *Chem. Lett.* **2006**, *35*, 352–353.
94. Tabata, M.; Maeda, K.; Higashi, M.; Lu, D.; Takata, T.; Abe, R.; Domen, K. Modified Ta_3N_5 Powder as a Photocatalyst for O_2 Evolution in a Two-Step Water Splitting System with an Iodate/Iodide Shuttle Redox Mediator under Visible Light. *Langmuir* **2010**, *26*, 9161–9165. [CrossRef] [PubMed]
95. Qi, Y.; Chen, S.; Li, M.; Ding, Q.; Li, Z.; Cui, J.; Dong, B.; Zhang, F.; Li, C. Achievement of visible-light-driven Z-scheme overall water splitting using barium-modified Ta_3N_5 as a H_2-evolving photocatalyst. *Chem. Sci.* **2017**, *8*, 437–443. [CrossRef] [PubMed]
96. Wang, Z.; Seo, J.; Hisatomi, T.; Nakabayashi, M.; Xiao, J.; Chen, S.; Lin, L.; Pan, Z.; Krause, M.; Yin, N.; et al. Efficient visible-light-driven water oxidation by single-crystal Ta_3N_5 nanoparticles. *Nano Res.* **2022**. [CrossRef]
97. Wang, Z.; Inoue, Y.; Hisatomi, T.; Ishikawa, R.; Wang, Q.; Takata, T.; Chen, S.; Shibata, N.; Ikuhara, Y.; Domen, K. Overall water splitting by Ta_3N_5 nanorod single crystals grown on the edges of $KTaO_3$ particles. *Nat. Catal.* **2018**, *1*, 756–763. [CrossRef]
98. Xiao, M.; Wang, Z.; Luo, B.; Wang, S.; Wang, L. Enhancing photocatalytic activity of tantalum nitride by rational suppression of bulk, interface and surface charge recombination. *Appl. Catal. B Environ.* **2019**, *246*, 195–201. [CrossRef]
99. Chen, S.; Shen, S.; Liu, G.; Qi, Y.; Zhang, F.; Li, C. Interface Engineering of a CoO_x/Ta_3N_5 Photocatalyst for Unprecedented Water Oxidation Performance under Visible-Light-Irradiation. *Angew. Chem. Int. Ed.* **2015**, *54*, 3047–3051. [CrossRef] [PubMed]
100. Niu, B.; Xu, Z. A stable Ta_3N_5@PANI core-shell photocatalyst: Shell thickness effect, high-efficient photocatalytic performance and enhanced mechanism. *J. Catal.* **2019**, *371*, 175–184. [CrossRef]
101. Ma, S.S.K.; Hisatomi, T.; Maeda, K.; Moriya, Y.; Domen, K. Enhanced Water Oxidation on Ta_3N_5 Photocatalysts by Modification with Alkaline Metal Salts. *J. Am. Chem. Soc.* **2012**, *134*, 19993–19996. [CrossRef] [PubMed]
102. Tang, R.; Zhou, S.; Zhang, Z.; Zheng, R.; Huang, J. Engineering Nanostructure–Interface of Photoanode Materials Toward Photoelectrochemical Water Oxidation. *Adv. Mater.* **2021**, *33*, 2005389. [CrossRef] [PubMed]
103. Zhang, K.; Ma, M.; Li, P.; Wang, D.H.; Park, J.H. Water Splitting Progress in Tandem Devices: Moving Photolysis beyond Electrolysis. *Adv. Energy Mater.* **2016**, *6*, 1600602. [CrossRef]
104. Higashi, M.; Domen, K.; Abe, R. Fabrication of efficient TaON and Ta_3N_5 photoanodes for water splitting under visible light irradiation. *Energy Environ. Sci.* **2011**, *4*, 4138–4147. [CrossRef]
105. Liao, M.; Feng, J.; Luo, W.; Wang, Z.; Zhang, J.; Li, Z.; Yu, T.; Zou, Z. Co_3O_4 Nanoparticles as Robust Water Oxidation Catalysts Towards Remarkably Enhanced Photostability of a Ta_3N_5 Photoanode. *Adv. Funct. Mater.* **2012**, *22*, 3066–3074. [CrossRef]
106. Dang, H.X.; Hahn, N.T.; Park, H.S.; Bard, A.J.; Mullins, C.B. Nanostructured Ta_3N_5 Films as Visible-Light Active Photoanodes for Water Oxidation. *J. Phys. Chem. C* **2012**, *116*, 19225–19232. [CrossRef]
107. Feng, X.; LaTempa, T.J.; Basham, J.I.; Mor, G.K.; Varghese, O.K.; Grimes, C.A. Ta_3N_5 Nanotube Arrays for Visible Light Water Photoelectrolysis. *Nano Lett.* **2010**, *10*, 948–952. [CrossRef]
108. Cong, Y.; Park, H.S.; Wang, S.; Dang, H.X.; Fan, F.-R.F.; Mullins, C.B.; Bard, A.J. Synthesis of Ta_3N_5 Nanotube Arrays Modified with Electrocatalysts for Photoelectrochemical Water Oxidation. *J. Phys. Chem. C* **2012**, *116*, 14541–14550. [CrossRef]
109. Zhen, C.; Wang, L.; Liu, G.; Lu, G.Q.; Cheng, H.-M. Template-free synthesis of Ta_3N_5 nanorod arrays for efficient photoelectrochemical water splitting. *Chem. Commun.* **2013**, *49*, 3019–3021. [CrossRef]
110. Li, Y.; Takata, T.; Cha, D.; Takanabe, K.; Minegishi, T.; Kubota, J.; Domen, K. Vertically Aligned Ta_3N_5 Nanorod Arrays for Solar-Driven Photoelectrochemical Water Splitting. *Adv. Mater.* **2013**, *25*, 125–131. [CrossRef]
111. Fu, J.; Fan, Z.; Nakabayashi, M.; Ju, H.; Pastukhova, N.; Xiao, Y.; Feng, C.; Shibata, N.; Domen, K.; Li, Y. Interface engineering of Ta_3N_5 thin film photoanode for highly efficient photoelectrochemical water splitting. *Nat. Commun.* **2022**, *13*, 729. [CrossRef] [PubMed]
112. Seo, J.; Takata, T.; Nakabayashi, M.; Hisatomi, T.; Shibata, N.; Minegishi, T.; Domen, K. Mg–Zr Cosubstituted Ta_3N_5 Photoanode for Lower-Onset-Potential Solar-Driven Photoelectrochemical Water Splitting. *J. Am. Chem. Soc.* **2015**, *137*, 12780–12783. [CrossRef] [PubMed]
113. Liu, G.; Ye, S.; Yan, P.; Xiong, F.; Fu, P.; Wang, Z.; Chen, Z.; Shi, J.; Li, C. Enabling an integrated tantalum nitride photoanode to approach the theoretical photocurrent limit for solar water splitting. *Energy Environ. Sci.* **2016**, *9*, 1327–1334. [CrossRef]
114. Shao, C.; Chen, R.; Zhao, Y.; Li, Z.; Zong, X.; Li, C. Reducing the surface defects of Ta_3N_5 photoanode towards enhanced photoelectrochemical water oxidation. *J. Mater. Chem. A* **2020**, *8*, 23274–23283. [CrossRef]
115. Xiao, Y.; Feng, C.; Fu, J.; Wang, F.; Li, C.; Kunzelmann, V.F.; Jiang, C.-M.; Nakabayashi, M.; Shibata, N.; Sharp, I.D.; et al. Band structure engineering and defect control of Ta_3N_5 for efficient photoelectrochemical water oxidation. *Nat. Catal.* **2020**, *3*, 932–940. [CrossRef]
116. Zhong, M.; Hisatomi, T.; Sasaki, Y.; Suzuki, S.; Teshima, K.; Nakabayashi, M.; Shibata, N.; Nishiyama, H.; Katayama, M.; Yamada, T.; et al. Highly Active GaN-Stabilized Ta_3N_5 Thin-Film Photoanode for Solar Water Oxidation. *Angew. Chem. Int. Ed.* **2017**, *56*, 4739–4743. [CrossRef] [PubMed]

117. Yang, L.; Fu, Q.; Wang, L.; Yu, J.; Xu, X. Liberating photocarriers in mesoporous single-crystalline $SrTaO_2N$ for efficient solar water splitting. *Appl. Catal. B Environ.* **2022**, *304*, 120934. [CrossRef]
118. Li, H.; Xiao, J.; Vequizo, J.J.M.; Hisatomi, T.; Nakabayashi, M.; Pan, Z.; Shibata, N.; Yamakata, A.; Takata, T.; Domen, K. One-Step Excitation Overall Water Splitting over a Modified Mg-Doped $BaTaO_2N$ Photocatalyst. *ACS Catal.* **2022**, *12*, 10179–10185. [CrossRef]
119. Wei, S.; Xu, X. Boosting photocatalytic water oxidation reactions over strontium tantalum oxynitride by structural laminations. *Appl. Catal. B Environ.* **2018**, *228*, 10–18. [CrossRef]
120. Zhang, H.; Wei, S.; Xu, X. Mg modified $BaTaO_2N$ as an efficient visible-light-active photocatalyst for water oxidation. *J. Catal.* **2020**, *383*, 135–143. [CrossRef]
121. Chen, K.; Xiao, J.; Vequizo, J.J.M.; Hisatomi, T.; Ma, Y.; Nakabayashi, M.; Takata, T.; Yamakata, A.; Shibata, N.; Domen, K. Overall Water Splitting by a $SrTaO_2N$-Based Photocatalyst Decorated with an Ir-Promoted Ru-Based Cocatalyst. *J. Am. Chem. Soc.* **2023**, *145*, 3839–3843. [CrossRef] [PubMed]
122. Wang, Z.; Luo, Y.; Hisatomi, T.; Vequizo, J.J.M.; Suzuki, S.; Chen, S.; Nakabayashi, M.; Lin, L.; Pan, Z.; Kariya, N.; et al. Sequential cocatalyst decoration on $BaTaO_2N$ towards highly-active Z-scheme water splitting. *Nat. Commun.* **2021**, *12*, 1005. [CrossRef] [PubMed]
123. Nishimae, S.; Vequizo, J.J.M.; Inoue, Y.; Yamakata, A.; Nakabayashi, M.; Higashi, T.; Domen, K. Active $BaTaO_2N$ photocatalysts prepared from an amorphous Ta_2O_5 precursor for overall water splitting under visible light. *J. Mater. Chem. A* **2023**, *11*, 6299–6310. [CrossRef]
124. Dong, B.; Cui, J.; Gao, Y.; Qi, Y.; Zhang, F.; Li, C. Heterostructure of 1D Ta_3N_5 Nanorod/$BaTaO_2N$ Nanoparticle Fabricated by a One-Step Ammonia Thermal Route for Remarkably Promoted Solar Hydrogen Production. *Adv. Mater.* **2019**, *31*, 1808185. [CrossRef] [PubMed]
125. Higashi, M.; Abe, R.; Teramura, K.; Takata, T.; Ohtani, B.; Domen, K. Two step water splitting into H_2 and O_2 under visible light by $ATaO_2N$ (A=Ca, Sr, Ba) and WO_3 with IO_3^-/I^- shuttle redox mediator. *Chem. Phys. Lett.* **2008**, *452*, 120–123. [CrossRef]
126. Higashi, M.; Abe, R.; Takata, T.; Domen, K. Photocatalytic Overall Water Splitting under Visible Light Using $ATaO_2N$ (A = Ca, Sr, Ba) and WO_3 in a IO_3^-/I^- Shuttle Redox Mediated System. *Chem. Mater.* **2009**, *21*, 1543–1549. [CrossRef]
127. Kasahara, A.; Nukumizu, K.; Takata, T.; Kondo, J.N.; Hara, M.; Kobayashi, H.; Domen, K. $LaTiO_2N$ as a Visible-Light (≤600 nm)-Driven Photocatalyst (2). *J. Phys. Chem. B* **2003**, *107*, 791–797. [CrossRef]
128. Li, Y.; Cheng, X.; Ruan, X.; Song, H.; Lou, Z.; Ye, Z.; Zhu, L. Enhancing photocatalytic activity for visible-light-driven H_2 generation with the surface reconstructed $LaTiO_2N$ nanostructures. *Nano Energy* **2015**, *12*, 775–784. [CrossRef]
129. Kasahara, A.; Nukumizu, K.; Hitoki, G.; Takata, T.; Kondo, J.N.; Hara, M.; Kobayashi, H.; Domen, K. Photoreactions on $LaTiO_2N$ under Visible Light Irradiation. *J. Mater. Chem. A* **2002**, *106*, 6750–6753. [CrossRef]
130. Zhang, Y.; Shi, J.; Cheng, C.; Zong, S.; Geng, J.; Guan, X.; Guo, L. Hydrothermal growth of $Co_3(OH)_2(HPO4)_2$ nano-needles on $LaTiO_2N$ for enhanced water oxidation under visible-light irradiation. *Appl. Catal. B Environ.* **2018**, *232*, 268–274. [CrossRef]
131. Wu, F.; Liu, G.; Xu, X. Efficient photocatalytic oxygen production over Ca-modified $LaTiO_2N$. *J. Catal.* **2017**, *346*, 10–20. [CrossRef]
132. Burns, E.; Aschauer, U.; Döbeli, M.; Schneider, C.W.; Pergolesi, D.; Lippert, T. $LaTiO_2N$ crystallographic orientation control significantly increases visible-light induced charge extraction. *J. Mater. Chem. A* **2020**, *8*, 22867–22873. [CrossRef]
133. Zhang, F.; Yamakata, A.; Maeda, K.; Moriya, Y.; Takata, T.; Kubota, J.; Teshima, K.; Oishi, S.; Domen, K. Cobalt-Modified Porous Single-Crystalline $LaTiO_2N$ for Highly Efficient Water Oxidation under Visible Light. *J. Am. Chem. Soc.* **2012**, *134*, 8348–8351. [CrossRef]
134. Xiong, F.-Q.; Dong, B.; Yu, S. Particulate Oxynitride Photoanodes Assembled with Transparent Electron-Collecting Oxide Nanorod Arrays. *Inorg. Chem.* **2019**, *58*, 13108–13114. [CrossRef]
135. Abdulla-Al-Mamun, M.; Rahman, M.M.; Shamsuddin, S.M. Dual cocatalysts induced photocurrent enhancement of $LaTiO_2N$ photoanode. *Mater. Lett.* **2019**, *245*, 147–150. [CrossRef]
136. Minegishi, T.; Nishimura, N.; Kubota, J.; Domen, K. Photoelectrochemical properties of $LaTiO_2N$ electrodes prepared by particle transfer for sunlight-driven water splitting. *Chem. Sci.* **2013**, *4*, 1120–1124. [CrossRef]
137. Akiyama, S.; Nakabayashi, M.; Shibata, N.; Minegishi, T.; Asakura, Y.; Abdulla-Al-Mamun, M.; Hisatomi, T.; Nishiyama, H.; Katayama, M.; Yamada, T.; et al. Highly Efficient Water Oxidation Photoanode Made of Surface Modified $LaTiO_2N$ Particles. *Small* **2016**, *12*, 5468–5476. [CrossRef] [PubMed]
138. Chae, S.Y.; Yoon, N.; Park, E.D.; Joo, O.S. Surface modification of $CuInS_2$ photocathodes with ruthenium co-catalysts for efficient solar water splitting. *Appl. Surf. Sci.* **2023**, *612*, 155856. [CrossRef]
139. Li, M.; Chen, L.; Su, Y.; Yin, H.; Hu, K. Hexagonally ordered microbowl arrays decorated with ultrathin $CuInS_2$ nanosheets for enhanced photoelectrochemical performance. *J. Energy Chem.* **2020**, *51*, 134–142. [CrossRef]
140. Takashima, T.; Fujishiro, Y.; Irie, H. Noble Metal Modification of CdS-Covered $CuInS_2$ Electrodes for Improved Photoelectrochemical Activity and Stability. *Catalysts* **2020**, *10*, 949. [CrossRef]
141. Zheng, L.; Xu, Y.; Song, Y.; Wu, C.; Zhang, M.; Xie, Y. Nearly Monodisperse $CuInS_2$ Hierarchical Microarchitectures for Photocatalytic H_2 Evolution under Visible Light. *Inorg. Chem.* **2009**, *48*, 4003–4009. [CrossRef] [PubMed]
142. Ikeda, S.; Nakamura, T.; Lee, S.M.; Yagi, T.; Harada, T.; Minegishi, T.; Matsumura, M. Photoreduction of Water by using Modified $CuInS_2$ Electrodes. *ChemSusChem* **2011**, *4*, 262–268. [CrossRef]

143. Ishikawa, A.; Takata, T.; Kondo, J.N.; Hara, M.; Kobayashi, H.; Domen, K. Oxysulfide $Sm_2Ti_2S_2O_5$ as a Stable Photocatalyst for Water Oxidation and Reduction under Visible Light Irradiation ($\lambda \leq 650$ nm). *J. Am. Chem. Soc.* **2002**, *124*, 13547–13553. [CrossRef]
144. Ishikawa, A.; Yamada, Y.; Takata, T.; Kondo, J.N.; Hara, M.; Kobayashi, H.; Domen, K. Novel Synthesis and Photocatalytic Activity of Oxysulfide $Sm_2Ti_2S_2O_5$. *Chem. Mater.* **2003**, *15*, 4442–4446. [CrossRef]
145. Ishikawa, A.; Takata, T.; Matsumura, T.; Kondo, J.N.; Hara, M.; Kobayashi, H.; Domen, K. Oxysulfides $Ln_2Ti_2S_2O_5$ as Stable Photocatalysts for Water Oxidation and Reduction under Visible-Light Irradiation. *J. Phys. Chem. B* **2004**, *108*, 2637–2642. [CrossRef]
146. Kiyonori, O.; Akio, I.; Kentaro, T.; Kenji, T.; Michikazu, H.; Kazunari, D. Lanthanum–Indium Oxysulfide as a Visible Light Driven Photocatalyst for Water Splitting. *Chem. Lett.* **2007**, *36*, 854–855.
147. Ogisu, K.; Ishikawa, A.; Shimodaira, Y.; Takata, T.; Kobayashi, H.; Domen, K. Electronic Band Structures and Photochemical Properties of La−Ga-based Oxysulfides. *J. Phys. Chem. C* **2008**, *112*, 11978–11984. [CrossRef]
148. Zhang, F.; Maeda, K.; Takata, T.; Domen, K. Improvement of the photocatalytic hydrogen evolution activity of $Sm_2Ti_2S_2O_5$ under visible light by metal ion additives. *J. Catal.* **2011**, *280*, 1–7. [CrossRef]
149. Zhao, W.; Maeda, K.; Zhang, F.; Hisatomi, T.; Domen, K. Effect of post-treatments on the photocatalytic activity of $Sm_2Ti_2S_2O_5$ for the hydrogen evolution reaction. *Phys. Chem. Chem. Phys.* **2014**, *16*, 12051–12056. [CrossRef]
150. Tuc Altaf, C.; Abdullayeva, N.; Coskun, O.; Kumtepe, A.; Yildirim, İ.D.; Erdem, E.; Liu, M.; Bozbey, A.; Agar, E.; Sankir, M.; et al. Efficiency enhancement in photoelectrochemical water splitting: Defect passivation and boosted charge transfer kinetics of zinc oxide nanostructures via chalcopyrite/chalcogenide mix sensitization. *Phys. Rev. Mater.* **2021**, *5*, 125403. [CrossRef]
151. Marsen, B.; Cole, B.; Miller, E.L. Photoelectrolysis of water using thin copper gallium diselenide electrodes. *Sol. Energy Mater. Sol. Cells* **2008**, *92*, 1054–1058. [CrossRef]
152. Moriya, M.; Minegishi, T.; Kumagai, H.; Katayama, M.; Kubota, J.; Domen, K. Stable Hydrogen Evolution from CdS-Modified $CuGaSe_2$ Photoelectrode under Visible-Light Irradiation. *J. Am. Chem. Soc.* **2013**, *135*, 3733–3735. [CrossRef] [PubMed]
153. Yokoyama, D.; Minegishi, T.; Maeda, K.; Katayama, M.; Kubota, J.; Yamada, A.; Konagai, M.; Domen, K. Photoelectrochemical water splitting using a Cu (In, Ga) Se_2 thin film. *Electrochem. Commun.* **2010**, *12*, 851–853. [CrossRef]
154. Prasad, G.; Srivastava, O.N. The high-efficiency (17.1%) WSe_2 photo-electrochemical solar cell. *J. Phys. D: Appl. Phys.* **1988**, *21*, 1028. [CrossRef]
155. McKone, J.R.; Pieterick, A.P.; Gray, H.B.; Lewis, N.S. Hydrogen Evolution from Pt/Ru-Coated p-Type WSe_2 Photocathodes. *J. Am. Chem. Soc.* **2013**, *135*, 223–231. [CrossRef]
156. Bozheyev, F.; Fengler, S.; Kollmann, J.; Klassen, T.; Schieda, M. Transient Surface Photovoltage Spectroscopy of $(NH_4)_2Mo_3S_{13}/WSe_2$ Thin-Film Photocathodes for Photoelectrochemical Hydrogen Evolution. *ACS Appl. Mater. Interfaces* **2022**, *14*, 22071–22081. [CrossRef]
157. Xi, F.; Bozheyev, F.; Han, X.; Rusu, M.; Rappich, J.; Abdi, F.F.; Bogdanoff, P.; Kaltsoyannis, N.; Fiechter, S. Enhancing Hydrogen Evolution Reaction via Synergistic Interaction between the $[Mo_3S_{13}]_2$– Cluster Co-Catalyst and WSe_2 Photocathode. *ACS Appl. Mater. Interfaces* **2022**, *14*, 52815–52824. [CrossRef]
158. Yu, X.; Guijarro, N.; Johnson, M.; Sivula, K. Defect Mitigation of Solution-Processed 2D WSe_2 Nanoflakes for Solar-to-Hydrogen Conversion. *Nano Lett.* **2018**, *18*, 215–222. [CrossRef]
159. Narangari, P.R.; Butson, J.D.; Tan, H.H.; Jagadish, C.; Karuturi, S. Surface-Tailored InP Nanowires via Self-Assembled Au Nanodots for Efficient and Stable Photoelectrochemical Hydrogen Evolution. *Nano Lett.* **2021**, *21*, 6967–6974. [CrossRef]
160. Gao, L.; Cui, Y.; Vervuurt, R.H.J.; van Dam, D.; van Veldhoven, R.P.J.; Hofmann, J.P.; Bol, A.A.; Haverkort, J.E.M.; Notten, P.H.L.; Bakkers, E.P.A.M.; et al. High-Efficiency InP-Based Photocathode for Hydrogen Production by Interface Energetics Design and Photon Management. *Adv. Funct. Mater.* **2016**, *26*, 679–686. [CrossRef]
161. Heller, A.; Vadimsky, R.G. Efficient Solar to Chemical Conversion: 12% Efficient Photoassisted Electrolysis in the [p-type InP(Ru)]/HCl-KCl/Pt(Rh) Cell. *Phys. Rev. Lett.* **1981**, *46*, 1153–1156. [CrossRef]
162. Lee, M.H.; Takei, K.; Zhang, J.; Kapadia, R.; Zheng, M.; Chen, Y.-Z.; Nah, J.; Matthews, T.S.; Chueh, Y.-L.; Ager, J.W.; et al. p-Type InP Nanopillar Photocathodes for Efficient Solar-Driven Hydrogen Production. *Angew. Chem. Int. Ed.* **2012**, *51*, 10760–10764. [CrossRef] [PubMed]
163. Zhang, X.; Ai, Z.; Jia, F.; Zhang, L. Generalized One-Pot Synthesis, Characterization, and Photocatalytic Activity of Hierarchical BiOX (X = Cl, Br, I) Nanoplate Microspheres. *J. Phys. Chem. C* **2008**, *112*, 747–753. [CrossRef]
164. Yang, J.; Su, H.; Wu, Y.; Li, D.; Zhang, D.; Sun, H.; Yin, S. Facile synthesis of kermesinus BiOI with oxygen vacancy for efficient hydrogen generation. *Chem. Eng. J.* **2021**, *420*, 127607. [CrossRef]
165. Zhang, B.; Wang, D.; Jiao, S.; Xu, Z.; Liu, Y.; Zhao, C.; Pan, J.; Liu, D.; Liu, G.; Jiang, B.; et al. TiO_2-X mesoporous nanospheres/BiOI nanosheets S-scheme heterostructure for high efficiency, stable and unbiased photocatalytic hydrogen production. *Chem. Eng. J.* **2022**, *446*, 137138. [CrossRef]
166. Hahn, N.T.; Hoang, S.; Self, J.L.; Mullins, C.B. Spray Pyrolysis Deposition and Photoelectrochemical Properties of n-Type BiOI Nanoplatelet Thin Films. *ACS Nano* **2012**, *6*, 7712–7722. [CrossRef]
167. Jeon, T.; Kim, S.J.; Yoon, J.; Byun, J.; Hong, H.R.; Lee, T.-W.; Kim, J.-S.; Shin, B.; Kim, S.O. Hybrid Perovskites: Effective Crystal Growth for Optoelectronic Applications. *Adv. Energy Mater.* **2017**, *7*, 1602596. [CrossRef]
168. Chen, J.; Dong, C.; Idriss, H.; Mohammed, O.F.; Bakr, O.M. Metal Halide Perovskites for Solar-to-Chemical Fuel Conversion. *Adv. Energy Mater.* **2020**, *10*, 1902433. [CrossRef]

169. Lin, C.-H.; Hu, L.; Guan, X.; Kim, J.; Huang, C.-Y.; Huang, J.-K.; Singh, S.; Wu, T. Electrode Engineering in Halide Perovskite Electronics: Plenty of Room at the Interfaces. *Adv. Mater.* **2022**, *34*, 2108616. [CrossRef]
170. Weber, D. CH3NH3PbX3, a Pb(II)-System with Cubic Perovskite Structure. *Naturforscher* **1978**, *33*, 1443–1445. [CrossRef]
171. Kojima, A.; Teshima, K.; Shirai, Y.; Miyasaka, T. Organometal Halide Perovskites as Visible-Light Sensitizers for Photovoltaic Cells. *J. Am. Chem. Soc.* **2009**, *131*, 6050–6051. [CrossRef] [PubMed]
172. Nazir, G.; Lee, S.-Y.; Lee, J.-H.; Rehman, A.; Lee, J.-K.; Seok, S.I.; Park, S.-J. Stabilization of Perovskite Solar Cells: Recent Developments and Future Perspectives. *Adv. Mater.* **2022**, *34*, 2204380. [CrossRef] [PubMed]
173. Grimm, J.A.A.; Zhou, H.; Properzi, R.; Leutzsch, M.; Bistoni, G.; Nienhaus, J.; List, B. Catalytic asymmetric synthesis of cannabinoids and menthol from neral. *Nature* **2023**, *615*, 634–639. [CrossRef] [PubMed]
174. Wang, H.; Wang, X.; Zhang, H.; Ma, W.; Wang, L.; Zong, X. Organic−inorganic hybrid perovskites: Game-changing candidates for solar fuel production. *Nano Energy* **2020**, *71*, 104647. [CrossRef]
175. Singh, S.; Chen, H.; Shahrokhi, S.; Wang, L.P.; Lin, C.-H.; Hu, L.; Guan, X.; Tricoli, A.; Xu, Z.J.; Wu, T. Hybrid Organic–Inorganic Materials and Composites for Photoelectrochemical Water Splitting. *ACS Energy Lett.* **2020**, *5*, 1487–1497. [CrossRef]
176. Pan, S.; Li, J.; Wen, Z.; Lu, R.; Zhang, Q.; Jin, H.; Zhang, L.; Chen, Y.; Wang, S. Halide Perovskite Materials for Photo(Electro)Chemical Applications: Dimensionality, Heterojunction, and Performance. *Adv. Energy Mater.* **2022**, *12*, 2004002. [CrossRef]
177. Chen, S.; Yin, H.; Liu, P.; Wang, Y.; Zhao, H. Stabilization and Performance Enhancement Strategies for Halide Perovskite Photocatalysts. *Adv. Mater.* **2023**, *35*, 2203836. [CrossRef]
178. Park, S.; Chang, W.J.; Lee, C.W.; Park, S.; Ahn, H.-Y.; Nam, K.T. Photocatalytic hydrogen generation from hydriodic acid using methylammonium lead iodide in dynamic equilibrium with aqueous solution. *Nat. Energy* **2016**, *2*, 16185. [CrossRef]
179. Wu, Y.; Wang, P.; Zhu, X.; Zhang, Q.; Wang, Z.; Liu, Y.; Zou, G.; Dai, Y.; Whangbo, M.-H.; Huang, B. Composite of $CH_3NH_3PbI_3$ with Reduced Graphene Oxide as a Highly Efficient and Stable Visible-Light Photocatalyst for Hydrogen Evolution in Aqueous HI Solution. *Adv. Mater.* **2018**, *30*, 1704342. [CrossRef] [PubMed]
180. Wang, X.; Wang, H.; Zhang, H.; Yu, W.; Wang, X.; Zhao, Y.; Zong, X.; Li, C. Dynamic Interaction between Methylammonium Lead Iodide and TiO_2 Nanocrystals Leads to Enhanced Photocatalytic H_2 Evolution from HI Splitting. *ACS Energy Lett.* **2018**, *3*, 1159–1164. [CrossRef]
181. Zhao, Z.; Wu, J.; Zheng, Y.-Z.; Li, N.; Li, X.; Tao, X. Ni_3C-Decorated $MAPbI_3$ as Visible-Light Photocatalyst for H_2 Evolution from HI Splitting. *ACS Catal.* **2019**, *9*, 8144–8152. [CrossRef]
182. Cai, C.; Teng, Y.; Wu, J.-H.; Li, J.-Y.; Chen, H.-Y.; Chen, J.-H.; Kuang, D.-B. In Situ Photosynthesis of an $MAPbI_3$/CoP Hybrid Heterojunction for Efficient Photocatalytic Hydrogen Evolution. *Adv. Funct. Mater.* **2020**, *30*, 2001478. [CrossRef]
183. Zhao, X.; Chen, S.; Yin, H.; Jiang, S.; Zhao, K.; Kang, J.; Liu, P.F.; Jiang, L.; Zhu, Z.; Cui, D.; et al. Perovskite Microcrystals with Intercalated Monolayer MoS_2 Nanosheets as Advanced Photocatalyst for Solar-Powered Hydrogen Generation. *Matter* **2020**, *3*, 935–949. [CrossRef]
184. Guan, W.; Li, Y.; Zhong, Q.; Liu, H.; Chen, J.; Hu, H.; Lv, K.; Gong, J.; Xu, Y.; Kang, Z.; et al. Fabricating $MAPbI_3$/MoS_2 Composites for Improved Photocatalytic Performance. *Nano Lett.* **2021**, *21*, 597–604. [CrossRef]
185. Da, P.; Cha, M.; Sun, L.; Wu, Y.; Wang, Z.-S.; Zheng, G. High-Performance Perovskite Photoanode Enabled by Ni Passivation and Catalysis. *Nano Lett.* **2015**, *15*, 3452–3457. [CrossRef]
186. Wang, C.; Yang, S.; Chen, X.; Wen, T.; Yang, H.G. Surface-functionalized perovskite films for stable photoelectrochemical water splitting. *J. Mater. Chem. A* **2017**, *5*, 910–913. [CrossRef]
187. Kim, I.S.; Pellin, M.J.; Martinson, A.B.F. Acid-Compatible Halide Perovskite Photocathodes Utilizing Atomic Layer Deposited TiO_2 for Solar-Driven Hydrogen Evolution. *ACS Energy Lett.* **2019**, *4*, 293–298. [CrossRef]
188. Hoang, M.T.; Pham, N.D.; Han, J.H.; Gardner, J.M.; Oh, I. Integrated Photoelectrolysis of Water Implemented On Organic Metal Halide Perovskite Photoelectrode. *ACS Appl. Mater. Interfaces* **2016**, *8*, 11904–11909. [CrossRef]
189. Poli, I.; Hintermair, U.; Regue, M.; Kumar, S.; Sackville, E.V.; Baker, J.; Watson, T.M.; Eslava, S.; Cameron, P.J. Graphite-protected $CsPbBr_3$ perovskite photoanodes functionalised with water oxidation catalyst for oxygen evolution in water. *Nat. Commun.* **2019**, *10*, 2097. [CrossRef]
190. Crespo-Quesada, M.; Pazos-Outón, L.M.; Warnan, J.; Kuehnel, M.F.; Friend, R.H.; Reisner, E. Metal-encapsulated organolead halide perovskite photocathode for solar-driven hydrogen evolution in water. *Nat. Commun.* **2016**, *7*, 12555. [CrossRef]
191. Nam, S.; Mai, C.T.K.; Oh, I. Ultrastable Photoelectrodes for Solar Water Splitting Based on Organic Metal Halide Perovskite Fabricated by Lift-Off Process. *ACS Appl. Mater. Interfaces* **2018**, *10*, 14659–14664. [CrossRef] [PubMed]
192. Andrei, V.; Hoye, R.L.Z.; Crespo-Quesada, M.; Bajada, M.; Ahmad, S.; De Volder, M.; Friend, R.; Reisner, E. Scalable Triple Cation Mixed Halide Perovskite–$BiVO_4$ Tandems for Bias-Free Water Splitting. *Adv. Energy Mater.* **2018**, *8*, 1801403. [CrossRef]
193. Gao, L.-F.; Luo, W.-J.; Yao, Y.-F.; Zou, Z.-G. An all-inorganic lead halide perovskite-based photocathode for stable water reduction. *Chem. Commun.* **2018**, *54*, 11459–11462. [CrossRef] [PubMed]
194. Zhang, H.; Yang, Z.; Yu, W.; Wang, H.; Ma, W.; Zong, X.; Li, C. A Sandwich-Like Organolead Halide Perovskite Photocathode for Efficient and Durable Photoelectrochemical Hydrogen Evolution in Water. *Adv. Energy Mater.* **2018**, *8*, 1800795. [CrossRef]
195. Jena, A.; Chen, C.-J.; Chang, H.; Hu, S.-F.; Liu, R.-S. Comprehensive view on recent developments in hydrogen evolution using MoS_2 on a Si photocathode: From electronic to electrochemical aspects. *J. Mater. Chem. A* **2021**, *9*, 3767–3785. [CrossRef]

196. Luo, Z.; Wang, T.; Gong, J. Single-crystal silicon-based electrodes for unbiased solar water splitting: Current status and prospects. *Chem. Soc. Rev.* **2019**, *48*, 2158–2181. [CrossRef]
197. Boettcher, S.W.; Spurgeon, J.M.; Putnam, M.C.; Warren, E.L.; Turner-Evans, D.B.; Kelzenberg, M.D.; Maiolo, J.R.; Atwater, H.A.; Lewis, N.S. Energy-Conversion Properties of Vapor-Liquid-Solid-Grown Silicon Wire-Array Photocathodes. *Science* **2010**, *327*, 185–187. [CrossRef] [PubMed]
198. Kelzenberg, M.D.; Boettcher, S.W.; Petykiewicz, J.A.; Turner-Evans, D.B.; Putnam, M.C.; Warren, E.L.; Spurgeon, J.M.; Briggs, R.M.; Lewis, N.S.; Atwater, H.A. Enhanced absorption and carrier collection in Si wire arrays for photovoltaic applications. *Nat. Mater.* **2010**, *9*, 239–244. [CrossRef]
199. Boettcher, S.W.; Warren, E.L.; Putnam, M.C.; Santori, E.A.; Turner-Evans, D.; Kelzenberg, M.D.; Walter, M.G.; McKone, J.R.; Brunschwig, B.S.; Atwater, H.A.; et al. Photoelectrochemical Hydrogen Evolution Using Si Microwire Arrays. *J. Am. Chem. Soc.* **2011**, *133*, 1216–1219. [CrossRef]
200. Oh, J.; Deutsch, T.G.; Yuan, H.-C.; Branz, H.M. Nanoporous black silicon photocathode for H_2 production by photoelectrochemical water splitting. *Energy Environ. Sci.* **2011**, *4*, 1690–1694. [CrossRef]
201. Oh, I.; Kye, J.; Hwang, S. Enhanced Photoelectrochemical Hydrogen Production from Silicon Nanowire Array Photocathode. *Nano Lett.* **2012**, *12*, 298–302. [CrossRef] [PubMed]
202. Bae, D.; Seger, B.; Vesborg, P.C.K.; Hansen, O.; Chorkendorff, I. Strategies for stable water splitting via protected photoelectrodes. *Chem. Soc. Rev.* **2017**, *46*, 1933–1954. [CrossRef] [PubMed]
203. Chen, Y.W.; Prange, J.D.; Dühnen, S.; Park, Y.; Gunji, M.; Chidsey, C.E.D.; McIntyre, P.C. Atomic layer-deposited tunnel oxide stabilizes silicon photoanodes for water oxidation. *Nat. Mater.* **2011**, *10*, 539–544. [CrossRef] [PubMed]
204. Seger, B.; Laursen, A.B.; Vesborg, P.C.K.; Pedersen, T.; Hansen, O.; Dahl, S.; Chorkendorff, I. Hydrogen Production Using a Molybdenum Sulfide Catalyst on a Titanium-Protected n+p-Silicon Photocathode. *Angew. Chem. Int. Ed.* **2012**, *51*, 9128–9131. [CrossRef] [PubMed]
205. Reece, S.Y.; Hamel, J.A.; Sung, K.; Jarvi, T.D.; Esswein, A.J.; Pijpers, J.J.H.; Nocera, D.G. Wireless Solar Water Splitting Using Silicon-Based Semiconductors and Earth-Abundant Catalysts. *Science* **2011**, *334*, 645–648. [CrossRef] [PubMed]
206. Warren, E.L.; McKone, J.R.; Atwater, H.A.; Gray, H.B.; Lewis, N.S. Hydrogen-evolution characteristics of Ni–Mo-coated, radial junction, n+p-silicon microwire array photocathodes. *Energy Environ. Sci.* **2012**, *5*, 9653–9661. [CrossRef]
207. Cox, C.R.; Winkler, M.T.; Pijpers, J.J.H.; Buonassisi, T.; Nocera, D.G. Interfaces between water splitting catalysts and buried silicon junctions. *Energy Environ. Sci.* **2013**, *6*, 532–538. [CrossRef]
208. Sun, K.; Park, N.; Sun, Z.; Zhou, J.; Wang, J.; Pang, X.; Shen, S.; Noh, S.Y.; Jing, Y.; Jin, S.; et al. Nickel oxide functionalized silicon for efficient photo-oxidation of water. *Energy Environ. Sci.* **2012**, *5*, 7872–7877. [CrossRef]
209. Young, E.R.; Costi, R.; Paydavosi, S.; Nocera, D.G.; Bulović, V. Photo-assisted water oxidation with cobalt-based catalyst formed from thin-film cobalt metal on silicon photoanodes. *Energy Environ. Sci.* **2011**, *4*, 2058–2061. [CrossRef]
210. Strandwitz, N.C.; Comstock, D.J.; Grimm, R.L.; Nielander, A.C.; Elam, J.; Lewis, N.S. Photoelectrochemical Behavior of n-type Si(100) Electrodes Coated with Thin Films of Manganese Oxide Grown by Atomic Layer Deposition. *J. Phys. Chem. C* **2013**, *117*, 4931–4936. [CrossRef]
211. Zhang, S.; Zhao, H.; Li, X.; Li, Y.; Jin, Y.; Liu, X.; Shi, G.; Wong, P.K. A hierarchical SiPN/CN/MoS_x photocathode with low internal resistance and strong light-absorption for solar hydrogen production. *Appl. Catal. B Environ.* **2022**, *300*, 120758. [CrossRef]
212. Meng, L.; He, J.; Tian, W.; Wang, M.; Long, R.; Li, L. Ni/Fe Codoped In_2S_3 Nanosheet Arrays Boost Photo-Electrochemical Performance of Planar Si Photocathodes. *Adv. Energy Mater.* **2019**, *9*, 1902135. [CrossRef]
213. Yao, T.; Chen, R.; Li, J.; Han, J.; Qin, W.; Wang, H.; Shi, J.; Fan, F.; Li, C. Manipulating the Interfacial Energetics of n-type Silicon Photoanode for Efficient Water Oxidation. *J. Am. Chem. Soc.* **2016**, *138*, 13664–13672. [CrossRef]
214. Ma, J.; Chi, H.; Wang, A.; Wang, P.; Jing, H.; Yao, T.; Li, C. Identifying and Removing the Interfacial States in Metal-Oxide–Semiconductor Schottky Si Photoanodes for the Highest Fill Factor. *J. Am. Chem. Soc.* **2022**, *144*, 17540–17548. [CrossRef] [PubMed]
215. Ritterskamp, P.; Kuklya, A.; Wüstkamp, M.-A.; Kerpen, K.; Weidenthaler, C.; Demuth, M. A Titanium Disilicide Derived Semiconducting Catalyst for Water Splitting under Solar Radiation—Reversible Storage of Oxygen and Hydrogen. *Angew. Chem. Int. Ed.* **2007**, *46*, 7770–7774. [CrossRef] [PubMed]
216. Zhang, C.; Liu, A.; Li, K.; Du, Y.; Yang, P. One-Step Synthesis of $MoS_2/TiSi_2$ via an In Situ Photo-Assisted Reduction Method for Enhanced Photocatalytic H_2 Evolution under Simulated Sunlight Illumination. *Catalysts* **2019**, *9*, 299. [CrossRef]
217. Banerjee, S.; Mohapatra, S.K.; Misra, M. Water Photooxidation by $TiSi_2$–TiO_2 Nanotubes. *J. Phys. Chem. C* **2011**, *115*, 12643–12649. [CrossRef]